

# Comprehensive Analysis of Coronal Mass Ejection Mass and Energy Properties Over a Full Solar Cycle

A.Vourlidas<sup>1</sup>, R. A. Howard<sup>1</sup>, E. Esfandiari<sup>2</sup>, S. Patsourakos<sup>3</sup>, S. Yashiro<sup>4</sup>, and G. Michalek<sup>5</sup>

## ABSTRACT

The LASCO coronagraphs, in continuous operation since 1995, have observed the evolution of the solar corona and coronal mass ejections (CMEs) over a full solar cycle with high quality images and regular cadence. This is the first time that such a dataset becomes available and constitutes a unique resource for the study of CMEs. In this paper, we present a comprehensive investigation of the solar cycle dependence on the CME mass and energy over a full solar cycle (1996-2009) including the first in-depth discussion of the mass and energy analysis methods and their associated errors. Our analysis provides several results worthy of further studies. It demonstrates the possible existence of two event classes; 'normal' CMEs reaching constant mass for  $> 10 R_{\odot}$  and 'pseudo' CMEs which disappear in the C3 FOV. It shows that the mass and energy properties of CME reach constant levels, and therefore should be measured, only above  $\sim 10R_{\odot}$ . The mass density ( $g/R_{\odot}^2$ ) of CMEs varies relatively little ( $<$  order of magnitude) suggesting that the majority of the mass originates from a small range in coronal heights. We find a sudden reduction in the CME mass in mid-2003 which may be related to a change in the electron content of the large scale corona and we uncover the presence of a six-month periodicity in the ejected mass from 2003 onwards.

*Subject headings:* Sun: activity – Sun: corona – Sun: coronal mass ejections – Sun: magnetic fields

## 1. Introduction

Coronal Mass Ejections (CMEs) have been observed since the 1970s but in the last 15 years they have moved to the forefront of coronal research as evidenced by hundreds of publications. This

---

<sup>1</sup>code 7663, Naval Research Laboratory, Washington, DC, USA.

<sup>2</sup>Adnet Systems Inc, Rockville, MD, USA

<sup>3</sup>University of Ioannina, Department of Physics, Section of Astrogophysic, Ioannina, Greece

<sup>4</sup>Center for Solar and Space Weather, Catholic University of America, Washington, DC, USA

<sup>5</sup>Astronomical Observatory of Jagiellonian University, Cracow, Poland

large amount of work is driven by the availability of continuous solar observations from the instrumentation aboard the SOHO mission (Domingo et al. 1995). The Large Angle and Spectroscopic Coronagraph (LASCO) suite (Brueckner et al. 1995), in particular, has revolutionized CME analysis with high cadence, high spatial resolution and high sensitivity observations of these events. Since the early phases of the mission, a concerted effort was initiated to generate a comprehensive event list based on visual inspection of the images and manual measurements of several CME properties such as speed, width, and position angle. The LASCO CME list grew to 14,000 events by mid-2009 and is the largest collection of CME properties readily available online. This resource has been used extensively to study various CME properties (St. Cyr et al. 2000; Yashiro et al. 2004; Gopalswamy et al. 2009). In 2008, the LASCO instruments reached another milestone. They provided the first ever CME database to cover a full solar cycle with a single instrument, thus opening investigations to the solar cycle dependence of CME properties (Gopalswamy et al. 2004; Cremades & St. Cyr 2007; Mittal et al. 2009) without having to worry about inter-instrument differences. Most of the previous statistical analyses have focused on the properties of speed, width, rate of occurrence and association with flares and other low coronal phenomena. These properties are most commonly used in CME research. In 2004, we added CME mass and kinetic energy measurements to the online list and they have been incorporated in some analyses (Gopalswamy et al. 2009; Mittal et al. 2009). However, CME mass and energy measurements are used rather infrequently in analysis of individual events, most likely because researchers are not familiar with the mass analysis methods. There has not been a comprehensive discussion of the procedures, assumptions, errors and limitations of CME mass and energy analysis except for some descriptions in our papers (Vourlidas et al. 2000, 2002; Subramanian & Vourlidas 2007) and a few past works (Hildner et al. 1975; Poland et al. 1981). The present paper aims to fill this gap in the CME literature (Sections 1-2). In Section 3, we describe the database of CME mass images and the associated mass and energy statistics. Only a small part of this information is included in the online LASCO CME list. While the mass and energy statistics have been briefly touched on in past studies, section 4 presents a detailed statistical analysis of the mass and energy properties expanding on the previous work of Howard et al. (1985) and Vourlidas et al. (2002). We discuss several aspects that emerge from the statistical analysis of such a large event sample such as solar cycle dependencies and the possible existence of ‘pseudo-CMEs’. We conclude in § 5.

## 2. Calculation of CME Mass

The white light emission of CMEs, and of the quiescent corona, arises from the scattering of photospheric light by coronal electrons. The emission is optically thin and therefore contains contributions from all electrons along a given line of sight (LOS). It is also linearly polarized. The emission mechanism, Thomson scattering, is well understood and the total and polarized brightness intensities can be easily calculated if the LOS electron distribution is known or can be estimated (Billings 1966; Hayes et al. 2001; Vourlidas & Howard 2006). Inversely, if the emission of a coronal feature is measured, then the number of electrons (and hence mass) can be estimated.

To measure the mass of a CME, we first need to separate the brightness contribution of the CME from the background coronal signal. Given the dynamic nature of the ejection, the best way to remove the background corona is to subtract a suitably chosen pre-event image from the image containing the CME. This has been the procedure for all mass measurements published to date (e.g., Stewart et al. 1974; Poland et al. 1981; Howard et al. 1985; Hundhausen et al. 1994; Vourlidas et al. 2002) and has been described before (Hundhausen et al. 1994; Vourlidas et al. 2000, 2002). In this paper, we provide a thorough description of the procedures for mass and energy analysis starting with an outline of the steps involved:

1. The time series of the CME are examined to select the CME images and a pre-event image that does not contain signatures of the CME or other disturbances (e.g., a previous CME) over the range of position angles occupied by the event in question. The pre-event image must also be close in time to the event to minimize solar rotation or evolutionary effects. We will return to these issues in the next section.
2. The CME and pre-event images are corrected for instrumental effects (e.g., flat-fielding, vignetting, exposure time variation, stray light, etc) and calibrated in mean solar brightness (MSB or  $B/B_{\odot}$ ) units to produce the so-called Level-1 images<sup>1</sup>.
3. The pre-event image is subtracted from the images containing the CME. The resulting images are now in units of excess MSB and correspond to a base-difference sequence, roughly speaking.
4. The excess brightness image is transformed to the number of excess electrons using the Thomson scattering equations (Billings 1966) and the assumption that all electrons lie on the plane of the sky (Section 2.1.4 for details). This assumption is driven by the unknown LOS distribution of the CME electrons and provides a convenient lower limit to their number.
5. The mass (per pixel) can then be calculated from the number of electrons by assuming a composition of 90% H and 10% He which corresponds to  $1.97 \times 10^{-24}$  g per electron (Hildner et al. 1975).
6. Finally, the CME mass is calculated by summing all pixels inside the CME region. The region can be defined in various ways depending on the objective. Most often, the observer outlines the CME manually as in Vourlidas et al. (2000) and Subramanian & Vourlidas (2007). We call this the 'region of interest (ROI) method'. Alternatively, one can define a sector based on the CME width and central position angle and the coronagraph occulter edge and height of the CME front. These observed parameters define the angular boundaries and the inner and outer radial boundaries, respectively. We call this the 'sector method' and is the method used for the measurements in this paper. A third option is to measure mass flow through a location

---

<sup>1</sup>Level-1 images are available online at the NRL LASCO webpage (<http://lasco-www.nrl.navy.mil>)

in the corona by defining a narrow (i.e., a few pixels wide) rectangular box, and position it tangent to the limb, at a given height. This setup emulates the observations of slit-based instruments, such as coronal spectrometers, and can be used to compare coronagraphic and spectroscopic observations as we have done in Ciaravella et al. (2003).

It is obvious that a number of assumptions enter in the final mass calculation. A top level assessment of the reliability of CME mass measurements, based on Thomson scattering properties (Vourlidas et al. 2000) and MHD simulations (Lugaz et al. 2005), has shown that the masses may be underestimated by  $\sim 2x$ .

### 2.1. Error Analysis of CME Mass Calculations

The calculation of the mass of a CME involves several analysis steps; the images have to be calibrated, subtracted and their intensities converted to mass values. Errors and assumptions are associated with every step. However, this procedure has never been described in detail before and several of the steps are general and applicable to other studies besides mass analysis. We use an actual example to structure the discussion.

We transform a C3 image, containing a CME snapshot, from its raw stage to a mass image (Figure 1). We chose C3 rather than C2 images because the C3 instrument has a larger field of view (FOV), CMEs are fainter and the influence of non-solar sources such as F-corona, stars and cosmic rays is larger. Therefore, errors in C3 masses are expected to be higher than in C2 and our error analysis provides a conservative upper bound. For the same reason, we have chosen a rather weak CME event occurring in the presence of bright background structures (i.e., streamers) which reflects the majority of cases in the LASCO database. The procedure to achieve the transformation from raw images to mass can be outlined as follows:

$$\frac{DN}{sec} \rightarrow \text{MSB} \rightarrow \text{Excess MSB} \rightarrow \text{No of } e^- \rightarrow g$$

Let us take a look at each one of these steps in detail.

#### 2.1.1. From DN to Brightness

After the telemetry data are received on the ground, they are unpacked, and reformatted by the LASCO pipeline and are stored in the database as Level-0.5 FITS files in units of Digital Numbers (DNs). The first step towards calculating CME masses is to calibrate the images (Morrill et al. 2006; Llebaria et al. 2006) to Level-1 or in other words, we convert them from DN to brightness units (per pixel) as follows

$$I = \frac{S}{t} * V * F_{cal} \tag{1}$$

where  $I$  is the brightness in mean solar brightness units (MSB),  $S$  the signal in the image (DN),  $t$  the exposure time in seconds,  $V$  the vignetting function, and  $F_{cal}$  is the calibration factor (MSB/DN/sec/pix) for the passband of the instrument. Note that there is a different calibration factor for each filter. MSB is a standard quantity in coronagraph data analysis and represents the ratio of the coronal brightness ( $B$ ) at a given pixel location to the average brightness of the solar disk ( $B_{\odot}$ ). Sometimes it is denoted as  $B/B_{\odot}$  but we will maintain the MSB notation here. The vignetting function is a property of the optical system measuring the amount of obscuration of the aperture due to the occulters and other stops, as a function of field angle. Its effect on the image corresponds to that of a radial density filter combined with spatial resolution degradation in the inner field of view. The calibration factor is initially determined on the ground and refined in-orbit through the analysis of stellar photometry. Details on these and other coronagraph calibrations can be found in Morrill et al. (2006); Llebaria et al. (2006). Equation (1) is a rather simplified description of the image calibration retaining only terms important for our discussion. The actual Level-1 calibration procedure implements a host of other corrections (e.g., stray light subtraction, roll to solar north, etc) which are of secondary importance here.

For the error analysis, we use the ratio of the standard deviation,  $\sigma_x$ , of a given quantity,  $x$ , over the quantity itself ( $\sigma_x/x$ ) and perform standard error propagation calculation to assign the final error. For Equation (1), the results are collected in Table 1. The signal in the image (when converted to photons) obeys photon statistics and is given by  $1/\sqrt{S}$ . Obviously, the error increases as a function of heliocentric distance as the CME gets fainter. The other errors have been discussed in Morrill et al. (2006). When we apply these error estimates in Equation (1), we find  $\frac{\sigma_I}{I} \approx 1.98\% - 2.3\%$ . In other words, the photometric accuracy of a single C3 image is extremely good, of the order of a few percent.

### 2.1.2. From MSB to Excess MSB

Although the individual Level-1 images are photometrically accurate and without instrumental defects, they are still difficult to use for analysis because the F-corona, the background streamer structure, and any remaining stray light component hinder the accurate detection of the faint CME boundaries. The F-corona becomes increasingly the dominant contributor to the observed signal above about 5-6  $R_{\odot}$  while streamers tend to affect the visibility in the inner corona. The most straightforward way to remove these effects is by subtracting an image which does not contain any CME signal. This pre-event image must be as close in time as possible to the CME to minimize effects from coronal evolution and should not contain brightness changes due to CME material (current or a previous CME) or CME-induced effects, such as streamer deflections. Any remaining stray light component will be completely removed as well. These requirements are not always easy to satisfy especially during active periods when up to 10 CMEs may erupt in a single day. Sometimes, a post-event image can be used, but this is more difficult to put into an automatic routine, because it is difficult to automatically determine the end-point of the CME event. In

practice, the user has to ensure that the pre-event image does not contain any defects or effects from other events only over the position angles covered by the CME in question. The rest of the image can contain other events or even missing telemetry blocks. The resulting image is referred to as an 'excess brightness' image and is given by

$$I_{CME} = I - I_{pre}, \quad \sigma_I/I \approx 4\% \quad (2)$$

where  $I$  and  $I_{pre}$  are the CME and pre-event image, respectively, and the error is propagated from the errors found in the previous section. The error is based on the implicit assumption that the errors in the two images are statistically independent. This is not a good assumption, however. There is a high degree of correlation between images since the location of streamers and even the position angles of other CMEs may be similar in the two images. It is very difficult to provide an analytical error estimate given the multitude of event sizes, and coronal topologies. Instead we use the actual signal statistics from the excess brightness image in our example. Figure 2 shows a radial profile across the CME and the undisturbed background ahead of the event labeled as 'sky background'. The signal levels are  $1.3 \pm 3.4 \times 10^{-13}$  MSB. In our experience, these levels (of the order of  $10^{-13}$  MSB) are very typical for C3 images. A more intuitive representation is in terms of SNR per pixel shown in the bottom panel of Figure 2. The CME is about 5-10 times brighter than the background in a running difference image. Again, this is a very typical value for an average CME event. We can calculate the error based on these numbers but this is again an overestimation. Rarely, if ever, does one need to calculate the CME mass for a single pixel. We almost always sum the mass (brightness in this case) over hundreds or thousands of pixels. In our example, the CME occupies  $\sim 38,000$  pixels resulting in total brightness of  $3.7 \times 10^{-8} \pm 2 \times 10^{-12}$  MSB. The corresponding values for the background are  $-1.7 \times 10^{-9} \pm 5 \times 10^{-13}$  MSB. The summation naturally minimizes the errors. We summarize the various methods and errors in Table 1. It is rather obvious that the subtraction of a pre-event image introduces insignificant errors, if the pre-event image is selected with care.

### 2.1.3. From Excess MSB to Excess Mass

At this stage, we have isolated the brightness due to the CME material from that of the background corona. We can then calculate the number of electrons using the Thomson scattering equations (Billings 1966). If we also know the composition of the CME plasma, then we can calculate the mass from

$$M_{CME} = I_{CME} * C_e * C_{plasma} \quad (3)$$

where  $C_e$  is obtained from Thomson scattering theory, discussed in the next section, and is the number of electrons per MSB and  $C_{plasma}$  the composition of the CME plasma. Traditionally, a composition of 10% He is assumed as a typical value for the corona (Hildner et al. 1975). In this case,  $C_{plasma} = 1.97 \times 10^{-24}$  g/electron. The actual composition may vary from event to event. For example, several events contain filament/prominence structure with likely chromospheric

densities and composition. However, most (if not all) of the cool material is heated to coronal temperatures quickly (Filippov & Koutchmy 2002). There is also very little evidence (e.g. from EUV dimmings) of significant material ejection from temperatures below a few  $10^5$  K (Bewsher et al. 2008). Coronagraph studies have shown that a large part of the ejected mass comes from the high corona (e.g., Andrews et al. 1999; Robbrecht et al. 2009). It is safe to assume that in an average CME, the majority of the plasma originates in the corona and/or it is fully ionized. But is the value of 10% He representative of such plasma? Recent in-situ analysis of ICME composition suggests a slightly lower contribution of 6% (Figure 3 in Reinard 2008). To be conservative, we assume the He composition of CMEs varies between 6% and 10% and the expected uncertainty is then 6%. So the effect of the composition variability on the mass calculations is of the same order of a few percent as the other factors discussed previously.

#### 2.1.4. Projection Effects

The remaining factor in Equation (3),  $C_e$  is also the one with the largest uncertainties. While the brightness of a single electron is straightforward to calculate using Thomson scattering theory, the emission is optically thin. As a result the observed brightness is the sum of the emission from all electrons along the line of sight (LOS). Since we do not know *a priori* the 3D electron distribution within the CME, we have to assume a distribution to derive the number of electrons from the observed excess brightness. The standard, and simplest, approach is to assume that all of the emission along a given LOS comes from electrons located on the Thomson Sphere, which is the location where the LOS is tangent to the radial from Sun center. For the relatively small elongations covered by the C3 FOV, and other coronagraphs with outer field limits  $< 30R_{\odot}$ , the Thomson Sphere and the sky plane (a sphere of radius 1 AU) are virtually coincident. The concept of the Thomson Sphere was introduced in Vourlidas & Howard (2006) to account for larger distances from the Sun.

In effect, we assume that the three-dimensional distribution of the CME mass is equivalent to its two-dimensional projection on the image plane having no longitudinal (along the LOS) extension. Although this may seem a strong assumption, it has well-understood effects on the mass calculation. First, it results in a convenient lower bound since an electron scatters most efficiently on the Thomson Surface, and hence the brightness is maximum at the Thomson surface. Therefore more electrons are required at larger angular distances from the Thomson surface to produce the same brightness (Figure 3). Second, the final mass is underestimated by only  $\sim 2x$  as was shown by calculations (Vourlidas et al. 2000), models (Lugaz et al. 2005) and more recently by stereoscopic mass measurements (Colaninno & Vourlidas 2009).

There is an intuitive way to understand why this simple-minded assumption provides such robust mass measurements. Let us consider the angular dependence of the Thomson scattering total brightness ( $B_{total}$ ) in Figure 3 (see also Hundhausen (1993), Appendix A). It is almost constant for the first  $20^\circ$  from the sky plane, dropping by only 20% at  $40^\circ$  and finally dipping below 50%

only after  $60^\circ$ . Since the brightness curves are symmetric relative to the sky plane ( $0^\circ$ ), they imply that the total brightness (and hence total mass) is the same irrespective of how the electrons are distributed along the LOS within a  $40^\circ$  cone. In other words, our assumption of all electrons on the sky plane results in an exact mass measurement for any  $\leq 40^\circ$ -wide CME propagating along the sky plane. Since the average CME size is about  $40^\circ$  (Yashiro et al. 2004), and larger events have a substantial fraction along the sky plane (with the possible exception of halo-CMEs), we can see why mass measurements, using the standard assumptions, represent a reliable estimate of the true CME mass.

Of course, not all CMEs propagate along the sky plane or have small widths. For these cases, we can evaluate the reliability of mass estimates using theoretical 'error' curves. For simplicity, we assume a uniform electron distribution along the LOS. Then we know the 'actual' CME mass for CMEs of any width and can calculate the 'observed' mass using the Thomson scattering equations and the sky-plane assumption. The ratio between the 'observed' and 'actual' masses is a measure of the expected error in the mass calculation and is plotted as a function of CME half-width in the left panel of Figure 4. The curves show calculations at a given projected heliocentric distance (commonly called impact radius) for both total and polarized brightness. The inner solid lines correspond to the lowest height ( $1.2 R_\odot$ ). The curves for heights  $> 5R_\odot$  are virtually indistinguishable from each other. It is clear that the high angular sensitivity of the polarized brightness emission leads to significant underestimation of the mass even for moderately wide CMEs and thus makes it unsuitable for CME mass analyses.

In the case of CMEs propagating away from the sky plane, Figure 4 (right panel) suggests that the masses are moderately underestimated reaching a factor of 3x in the extreme case of a  $60^\circ$ -wide CME propagating almost along the Sun-Earth line. It is possible to introduce a first-order correction by assuming that all the mass lies on a different angle than the sky plane. This angle should be the CME angle of propagation, if it is known, or if it can be derived from other observations. An obvious solution is to assume radial propagation from the source active region (Reiner et al. 2003; Kahler & Vourlidas 2005). This assumption improves the accuracy of the mass measurements relative to the sky-plane assumption out to about  $60^\circ$  but diverges rapidly beyond that angle and overestimates the mass by about 5x at  $80^\circ$  (Figure 4). Although this is a valid approach for the analysis of individual events, it is not desirable for a statistical analysis of large number of events since it results in both over and underestimation of the masses. Besides, it requires positional knowledge about the source regions for all the events which we do not possess. Thus, we retain the 'sky-plane' assumption for our analysis and noting that the masses of some events (partial or full halo-CMEs) may be underestimated by as much as a factor of 3. We note also that the emission from some CMEs is blocked by the occulter reducing the estimate of the total mass of those events.

These considerations affect also the energy calculations. For the potential energy, the error is the same as for the mass; an underestimate of a factor of 2. Both mass and speed enter in the kinetic energy equation and for both quantities the projection effects are the dominant factors. The most



severe speed projection effects will be associated with CMEs out of the sky plane such as halo and partial halo events. But we have excluded these events from our statistics and thus we expect only moderate projection effects. However, there is no way of knowing which of the thousands of events in our list are close to the sky plane. To calculate a conservative error in the speed measurements, we assume a maximum value of  $60^\circ$  of the sky plane which translates to a factor of  $1/\cos 70 = 2$  underestimate of the CME speed. Since both mass and speed are underestimated, so will be the kinetic energies. Hence, the kinetic energies can be as much as 8x higher and the potential as much as 2x. The total mechanical energy will then be as much as 8x. We should therefore consider our mass and energy values as lower limits to the real ones.

To summarize we demonstrated that instrumental effects, the coronal background and the CME plasma composition are, in general, insignificant contributors to errors in estimating the CME mass. Projection effects play the major role but even those can be reasonably estimated. Our conclusion is that the CME mass and energy values are lower bounds to the true values and they lead to underestimations of  $\sim 2x$  for the mass and potential energy, and  $\sim 8x$  for the kinetic energy.

## 2.2. LASCO Observations and CME Mass Database

So far, we have discussed the CME mass measurement procedures and errors associated with them. The procedures are easily automated and applied to large numbers of CMEs (e.g., Vourlidas et al. 2000). So we apply them to all observed CMEs starting from the height-time (HT) measurements in the LASCO CME database <sup>2</sup> and we refer to it as the CDAW CME list hereafter (Yashiro et al. 2004). As we describe in detail below, we have compiled a new database containing not only mass and energy measurements but also calibrated mass images for each CME image. We refer to our list as the NRL CME list, hereafter. To automate the mass measurements we made some important decisions at the beginning.

First, it is impractical to outline the CME extent by hand for every frame for thousands of CMEs, so we measure the total mass within a sector defined angularly by the reported width and central position angle (PA) and radially by the occulter edge (lower boundary) and the reported height of the CME front (outer boundary) plus one  $R_\odot$  to ensure that we include the CME front since the weak brightness of the front may lead to errors in locating it visually at large heliocentric distances.

Second, we pick a pre-event image automatically based on the time of the first C2 (or C3) image reported in the CDAW CME list. We search backwards in time for the first available C2 (or C3) image which is free of missing blocks along the predefined sector. If no image is found up to 6 hour prior, then the event is dropped from the list and an error log is created. A detailed

---

<sup>2</sup>[http://cdaw.gsfc.nasa.gov/CME\\_list](http://cdaw.gsfc.nasa.gov/CME_list)

examination of each CME to determine the best pre-event image (if it exists) is beyond the scope of this paper.

Third, we calculate the mass only for the images used for the height-time (HT) measurements, even though additional images may exist. In many cases, not all LASCO data were available at the time of the height-time (HT) measurements but they may be available now. Generally speaking, we do not update the mass measurements once an event has been measured successfully through the above steps. Also we try to maintain a close correspondence with the HT measurements for our statistics work, and therefore, we do not want to add mass measurements where no HT measurements exist.

Four, we want to discriminate between CMEs and solar wind 'blobs' (Sheeley et al. 1997) as both types of events exist in the CDAW CME list. It is generally accepted that blobs are the smallest, narrowest ejections detected in the coronagraphs. However, there is no consensus on how small can a CME be. Some CMEs can appear narrow because of projection effects. The properties of events with widths  $< 15^\circ - 20^\circ$  have been analyzed before with somewhat conflicting conclusions on whether they form part of the overall CME distribution (Gilbert et al. 2001) or not (Yashiro et al. 2003). Since it is not clear where the CME width cuts off and to avoid potential bias we have decided to exclude all narrow events ( $< 20^\circ$ ) from our subsequent analysis. This decision is further motivated by a sudden upturn on the number of entries in the CME list starting in 2004. Almost all of the newly added events are of small width, they are not CMEs and, in our opinion, they are skewing the overall statistics. Finally, we do not check for accuracy or re-measure any of the inputs from the CDAW CME list such as speed, position angle, CME front height, etc.

The mass CME database is constructed as follows. Our software procedures read in the HT files as they become available online, retrieve the corresponding C2 or C3 files from the LASCO database and calculate full resolution, pre-event-subtracted, mass files (in units of g) which are stored in our mass database at NRL. For each mass file, we sum the mass within the sector defined above and calculate the total mass, area, average mass density (g/pix), center-of-mass height, and potential and kinetic energies. The details of the calculations of the potential and kinetic energy have been published in Vourlidas et al. (2000) so we will not go into details here. The above measurements, for all frames of a given event, are stored in a separate text file. Many additional parameters can now be derived such as speed and acceleration of the center-of-mass, CME area as a function of height, etc. To demonstrate the wealth of information contained in our final CME database, we plot several parameters from a randomly chosen CME in Figure 5.

Here, we focus on the properties of the full CME sample rather than the evolution of a particular event. So we want to treat each event as an individual data point and therefore need to extract, for each event, a representative set of parameters at a single time frame. As we have shown before, CME mass tends to a constant value above about  $10R_\odot$  (Vourlidas et al. 2000; Colaninno & Vourlidas 2009) and few events show any significant accumulation out to the edge of the C3 FOV. So it is natural to assume that a representative point for each event is the time when the CME achieves

its maximum mass. We extract all parameters (speed, mass, energies, etc) at that time frame and proceed to analyze their statistics. The final entry for each CME contains the following data:

- From the CDAW list: speed, acceleration, position angle, width, front height.
- From the NRL list: mass, number of pixels (summed over to obtain the mass), average mass per pixel, sector boundaries, kinetic and potential energies, center-of-mass height and position angle, and filename.

It is obvious that many statistical studies can be undertaken with so many available variables, and we looked at several correlations. For the sake of brevity and clarity, we present only the most important results in the following section.

### 3. Statistical Results

The initial event list contains 14007 CMEs, from 22 January 1996 to 31 July 2009, the last date with HT and mass measurements available during the writing of this paper. After going through the mass calculations procedures we end up with a mass sample of 13388 events. For the analysis here, we need to remove from consideration events that may bias the analysis. So we remove events with (1) too few ( $\leq 3$ ) measurements, (2) events with negative mass which may indicate overlapping events, (3) small width events that may not be CMEs, and (4) wide events which may have a significant portion of their structures away from the sky-plane and narrow events. We therefore consider only events with  $120^\circ > \text{widths} > 20^\circ$ . The remaining sample contains 7668 CMEs, easily the largest calibrated CME sample ever considered.

#### 3.1. Duty Cycle Considerations

For an instrument, the observing duty cycle is defined as the percentage of the total observing time during a certain time period (e.g. day, carrington rotation, etc). For Earth-orbiting telescopes, which operate over a day-night orbit, the duty cycle is basically the length of the day orbit. By virtue of its location at L1, the LASCO instrument is observing the Sun continuously and we only need to consider interruptions due to instrument or spacecraft operations. Such corrections are necessary for the evaluation of CME occurrence rates and are regularly applied (St. Cyr et al. 2000; Cremades & St. Cyr 2007). Here, however, we are interested in a slightly different problem. We do not want to only know if a CME has occurred but whether it also satisfied the criteria for inclusion in the database. In the following, we present two other approaches for calculating the LASCO duty cycle.

For a CME to appear in the catalog, it must have a speed measurement (an HT plot). For a reliable CME speed, we must have three C3 measurements, at least. Then, the CME will be

included, if it has a speed,

$$v_{CME} \leq \frac{\Delta l}{ndt} \quad (4)$$

where  $\Delta l$  is the distance from the C3 occulter to the edge of the field of view (in km),  $n = 3$  the number of images, and  $dt$  the time between successive C3 images (cadence, in min). Next, we calculate  $dt$  for all C3 images acquired during the mission. There are 175,361 such images and we simply take the time difference between successive images based on the image header. The resulting histogram, in 1-hour bins, is shown in Figure 6. The y-axis is normalized to the total number of images and represents the percentage of events in each hourly bin. We see that 93.6% of C3 images are taken within one hour from each other. The plot shows that almost all of C3 observations (98.9%) have a cadence of two hours or less. Setting  $dt = 60$  min in Equation (4), we obtain  $v_{CME} = 1824$  km/sec. This result implies that all CMEs with speeds  $< 1824$  km/sec will be detected, measured, and will therefore appear in our statistics. A quick search of the entire CME catalog shows that only 52 out of 14,409 CMEs (0.4%) have speeds above 1824 km/sec. While these are important events, eliminating them from the statistics for this paper has an insignificant effect. Thus, for all practical purposes, C3 detects all CMEs with one hour cadence. Therefore, the overall LASCO duty cycle is 94%.

This duty cycle can be used for comparisons with other instruments (e.g, 66.7% for *Solwind*) over the length of the mission. But it does not capture information on finer time scales. CMEs follow the general activity cycle as a look in Figure 14 quickly reveals. The number of CMEs per Carrington rotation is quickly rising during the summer of 1998 (rotations 1938-1940) but there are months with low number of CMEs as well. Therefore, data gaps may have a varying effect on the statistics depending on the phase of the cycle. Although we do not pursue this here, future studies may find the duty cycle per Carrington rotation useful information.

To calculate the duty cycle per Carrington number we proceed as follows. We showed above that high-speed CMEs will be easily missed with a few hours observing gap but slow CMEs will not. So we go back to Equation (4) and try to estimate the minimum data gap for missing a CME, irrespective of its speed.

First, we define a minimum CME speed. We know that the slowest CMEs are the streamer-blowout types with typical speeds of  $\sim 200$  km/sec (Vourlidas et al. 2002). The CDAW catalog contains events with speeds around 100 km/sec but some of them are questionable. There are a number of outward mass motions that have speeds lower than 100 km/s. This speed is below the escape speed (216 km/sec), so that outgoing material slower than this, must be a quasi-equilibrium outflow. We believe that these slow events are significantly different from CMEs which are associated with a magnetic instability and energy release. In any case, we adopt the rather conservative speed of 100 km/sec which results in  $dt = 18$  hrs from Equation (4). Therefore, any data gap longer than 18 hrs will surely result in failure to detect all CMEs (for the purposes of inclusion in the database). Figure 7 shows the resulting duty cycle per Carrington rotation. The long data gaps due to spacecraft emergencies are immediately obvious but the duty cycle is well within 90%

for the majority of the mission. As a check of our procedure, we calculate the average duty cycle per Carrington rotation for the full time series. We end up with a duty cycle of 94% which is the same number calculated above from the time between successive C3 exposures.

### 3.2. Mass and Energy Distributions

The distributions of mass and energy are shown in Figure 8. The bin size is 0.2 dex for all quantities and the statistics are presented in Table 2. The CME masses extend between  $10^{11}$  and  $10^{17}$  g but either extreme is defined by a very small number of events. There are only 7 events with masses  $\geq 5 \times 10^{16}$  g. At the lower end, there are also only 16 events with masses less than  $5 \times 10^{11}$  g. The low values are usually caused by overlapping CMEs where the first event creates large areas of negative brightness against which the second event propagates. Such cases are impossible to measure reliably in an automated fashion and are difficult to exclude from the statistics if their masses are positive. Another contributor to small masses are events with only one or two frames in C2. We discuss them in § 3.4.

What type of distribution should we expect for the mass and energy measurements? Neither the mass nor the energy can be negative and both have large variances (i.e., the mass values extend over 5 orders of magnitude). Log-normal distributions arise frequently under such conditions (Limpert et al. 2001; Crow & Shimizu 1988). In addition, log-normal distributions are common in solar physics. They have been identified in the distribution of magnetic flux in the photosphere (Abramenko & Longcope 2005), the CME speeds (Yurchyshyn et al. 2005), and CME-associated flares (Aoki et al. 2003). All three of these parameters are related to CMEs, either directly or indirectly. It is, therefore, reasonable to expect the same behavior from CME masses and energies. In that case the logarithms of both quantities in Figure 8 should be normally distributed but they are not. The departure from the normal distribution seems to be caused by an excess of small values in both mass and energy measurements. The skewness in the distributions may be caused by either the existence of two populations (a low and high mass CME population, for example) or by the inclusion of biased samples in our statistics. To investigate this, we proceed as follows.

First, we fit the measurements with a normal curve as shown in Figure 9. Mathematically speaking, when the (normalized) probability function  $P$  of the logarithm of a random variable  $x$  is normally distributed with a mean  $\mu$ , and standard deviation of  $\sigma$  (see also Yurchyshyn et al. (2005); Limpert et al. (2001))

$$P = \exp -\left(\frac{\log x - \mu}{\sqrt{2}\sigma}\right)^2 \tag{5}$$

then the variable is log-normally distributed with probability density function  $f(x)$  as

$$f(x) = \frac{1}{x\sigma\sqrt{2\pi}} \exp -\left(\frac{\log x - \mu}{\sqrt{2}\sigma}\right)^2 \tag{6}$$

Here,  $\mu$  represents the geometric mean and the one  $\sigma$  range is given by  $[\mu/\sigma, \mu \cdot \sigma]$  and the  $2\sigma$  range by  $[\mu/\sigma^2, \mu \cdot \sigma^2]$ . Thus we apply a Gaussian fit using equation (5) to the logarithm of mass

(Figure 9, top left panel, red line). The data deviate from the normal fit at both high and low mass values but the excess of low mass events is especially obvious.

Then we apply a two-Gaussian fit which does a much better job in describing the distribution (blue dashed lines are the individual components, blue thick line is the sum). This would indicate that we may be dealing with two populations. As we discuss in detail in § 3.4, there are indeed two populations *when* the masses are plotted against their height.

To check whether the height where the measurement was taken introduces a bias, we repeat the fitting but exclude all events which reach their maximum mass at less than  $7 R_{\odot}$  (3579 events, middle panels) and at less than  $15 R_{\odot}$  (1704 events, bottom panels). It is obvious that the mass measurements approach a log-normal distribution (the logarithm of mass becomes more normally distributed) as the height of maximum mass is increased and there is no need for a two-Gaussian fit. The final parameters of the fit are shown in Table 3. Obviously, the height where the mass measurement is performed is biasing the results giving the impression of a two-CME population in Figure 9. Therefore, the height, and by direct implication, the field of view, matters for the proper measurement of CME properties. This is an important consideration for instrument builders and for comparisons among different coronagraphs.

We have noted repeatedly in the past that there is considerable evolution of the CME mass with height (Vourlidas et al. 2002; Colaninno & Vourlidas 2009). The mass tends to increase rapidly between  $2-7 R_{\odot}$  and reaches a plateau above about  $7-10 R_{\odot}$  (Figure 5). Hence, a maximum mass below  $\sim 10 R_{\odot}$  would imply insufficient FOV coverage, overlapping events or improper event identification (Sect 3.4). In all such cases, the measurements should be treated with caution. Measurements from coronagraphs with limited FOVs (e.g.,  $\leq 10 R_{\odot}$ ) are especially affected. We conclude that *only CME measurements to at least  $15 R_{\odot}$  can allow the proper measurement of CME properties such as mass and energy.*

We use the same approach for the fitting of the kinetic energy (middle column, Figure 9) and total mechanical energy (right column, Figure 9). The results of the fit are shown in Table 3. The behavior is similar but not as striking as in the case of mass. The log-normal fit is better for the total energy than the kinetic energy, where an excess of low kinetic energy events is seen even at  $15 R_{\odot}$ . We do not know the exact reason for this. Since the kinetic energy is the product of the mass and speed measurements it should be distributed log-normally. However, we use the final *fitted* speeds provided in the CDAW catalog and not the speeds at the height where the mass measurements are taken. In principle, there should be a small difference, if any, for constant speed events but a significant one for decelerating or accelerating events. The excess of small kinetic energies at  $15 R_{\odot}$  suggests that their actual speed at  $15 R_{\odot}$  may be higher than their fitted constant speed, which is more representative of the speed at  $30 R_{\odot}$ . It is plausible that these events may tend to decelerate in the C3 FOV. However, a proper answer will require careful speed measurements for a large number of these events. We leave this exercise for another paper.

We close this section with a comparison of the LASCO mass distribution to *Solwind* dis-

tribution (Jackson & Howard 1993). This is the only other published mass distribution we are aware of. Jackson & Howard (1993) used  $\sim 1000$  CMEs to construct a mass distribution between  $10^{15} - 5 \times 10^{16}$  g. Their distribution for  $M \geq 4 \times 10^{15}$  g was described well by the exponential law  $N_{CME} = 370e^{-9.43 \times 10^{-17}M}$ . We compare their fit (dash-dotted line) to the LASCO mass distribution in Figure 10. Clearly, it is biased towards higher masses by about half a decade. This is expected, given the lower sensitivity of *Solwind* relative to the LASCO coronagraphs. The dashed line shows a better exponential fit between  $4 \times 10^{14} - 5 \times 10^{16}$  g. The lower cutoff is taken at the mass value where the distribution dips to lower values and is one order of magnitude smaller than the Jackson & Howard (1993) cutoff. The new law is  $N_{CME} = 370.1e^{-2.3 \times 10^{-16}M}$  which is a factor of 3.9 below the *Solwind* fit and leads to correspondingly lower mass fluxes (Table 4). Jackson & Howard (1993) justified the exponential fit and the existence of a detection threshold (assumed at  $\sim 4 \times 10^{15}$  g) on the grounds that the downturn in the distribution towards the lower values was due to instrument sensitivity. As we demonstrate in this paper, the LASCO coronagraphs are perfectly capable of detecting events carrying as little as a few  $\times 10^{12}$  g so the observed downturn at around  $4 \times 10^{14}$  g is not due to instrumental effects but is intrinsic to the mechanism of the generation of CMEs. Although the high mass values are described well by an exponential, we see no reason to use anything other than a log-normal fit.

The difference in the mass distributions between LASCO and *Solwind* could be due to a systematic error in the mass estimates or it could reflect a real change in the average CME mass between the two solar cycles. The *Solwind* measurements incorporated CMEs of all widths, including halos, which might affect the histogram. Also *Solwind* CME masses were computed using a proxy based on the width of the CME and the apparent surface brightness. The method was described in Howard et al. (1985). Briefly, the mass of a small number of CMEs (15 events) was determined with the same method of preevent subtraction as the LASCO masses. Then the mass of each CME was divided by its width, which resulted in a mass per degree. An average mass per degree was computed for the three apparent brightness groups (Faint, Average, Bright). Those averaged mass per degree values were used to estimate the mass for all the *Solwind* events. The *Solwind* masses are tied to a set of events that were calibrated in the normal sense, and are consistent with the masses calculated with the *SMM* and *Skylab* coronagraphs. It seems very unlikely that the event selection or a systematic offset can explain the difference in the mass curves of Figure 10 while maintaining the same exponential behavior. We have to conclude that the CMEs observed by LASCO, while having the same shape to the distribution function are in fact *less massive than the CMEs from 1971-1990*. The downward trend in CME properties is reflected in the transition to cycle 24 as we will see in § 3.5.

### 3.3. The 'Average' CME

We note an interesting behavior in the height distribution of the maximum mass (Figure 11, top panel). The data points seem to separate into two populations. There is a 'low corona' population

located mostly in the C2 FOV, at heights below  $7R_{\odot}$  with higher masses and a population spread throughout the rest of the C3 FOV showing a slightly increasing mass with height. The latter is representative of the mass evolution of individual CMEs (Figure 1). The 'low corona' component is, however, unexpected. Part of the mass increase with height is due to the increase of the CME area as it expands in the outer corona (see previous section). To account for that, we divide the masses with the number of pixels used to measure them and then transform the area from pixels to physical units ( $\text{cm}^2$ ). Thus, we obtain the CME column mass density ( $\text{g}/\text{cm}^2$ ) and column electron density ( $\text{e}/\text{cm}^2$ ). We plot the latter in the middle panel of Figure 11. As we suspected, the mass increase was due to the increasing, i.e. more of the event becomes visible in the coronagraph field of view. CME area. The CME density curve is flat above about  $7 R_{\odot}$  with a scatter of only a factor of 10. Given the large number of event sizes, orientations and projections, the degree of flatness seems remarkable. The height spread can be easily understood when we consider that the CME mass tends to a constant value above about  $10 R_{\odot}$  (Figure 5 and Vourlidas et al. 2000; Colaninno & Vourlidas 2009). This implies that the rapid expansion and post-CME flows have largely ceased and we call the event 'mature' at this point. However, the mass measurements are not absolutely flat but have some fluctuations. Since we pick the maximum mass automatically, this 'noise' will naturally result in a height spread. A more sophisticated selection criterion, such as fitting the individual event mass curves and picking the  $1/e$  values (as in Colaninno & Vourlidas 2009), should result in a much smaller spread.

Next we bin the data above  $10 R_{\odot}$  in  $1 R_{\odot}$ -wide bins and derive the average and standard deviation of the quantities in each bin. Fitting these points with a straight line results in the average density

$$\langle N_e \rangle = 10^{14.84 \pm 0.26} \text{ e}^- \text{ cm}^{-2}$$

or in terms of mass density,  $\rho$

$$\langle \rho \rangle = 10^{12.83 \pm 0.25} \text{ g}/R_{\odot}^2$$

We see that the spread in the densities is only a factor of about 3 which is much less than the four order of magnitude spread in the measured CME masses. It clear that, once the event has 'matured', the average CME density is rather constant and the observed variation in masses and consequently shapes and morphologies is mostly the result of projection effects rather than properties of the source region.

As an extension of the above discussion, we can estimate the volumetric CME electron density assuming that the LOS depth is equal to the projected angular CME width. For a sector with radial extent between radii,  $R_1$ , and  $R_2$  and angular extent between position angles,  $\theta_1$ , and  $\theta_2$ , or width,  $\Delta\theta = \theta_1 - \theta_2$ , the CME volume,  $V_{CME}$  is given by

$$v_{CME} = \frac{2}{3}(R_2^3 - R_1^3)\Delta\theta \sin \frac{(\theta_2 - \theta_1)}{2} \sin \frac{(\theta_2 + \theta_1)}{2} \quad (7)$$

The result is shown in the bottom plot of Figure 11. The volume density plot is similar to the other two except for a slight negative slope towards larger heights. This is expected on Thomson



scattering considerations. As the CME expands, it becomes fainter due to the  $R^{-2}$  dependence of the scattering, especially for the parts away from the sky plane. When their brightness reaches background levels, it stops contributing to the total CME brightness. The very shallow drop, however, even at  $30 R_{\odot}$  is a testament to the high sensitivity of the C3 coronagraph. The average CME electron density is then

$$\langle n_e \rangle = 10^{3.55 \pm 0.29} \text{ e}^{-} \text{ cm}^{-3}$$

Again, the spread in the volume density is only a factor of 3.8. This result, based on statistics of several 1000s of events, suggests, rather strongly in our opinion, that there is very small variation in the mass densities of the ejected plasma and that the plasma must come from higher altitudes where there is less density variation compared to the low corona. For example, if we assume that CMEs expand adiabatically in the corona, their density should drop as  $R^{-3}$ . Since we find that the events reach a more or less constant density at  $10 - 15 R_{\odot}$ , their original density, on average, on the surface ( $\sim 1 R_{\odot}$ ) should be  $\sim 3.5 - 12 \times 10^6 \text{ cm}^{-3}$ . However, these values are 2 to 3 orders of magnitude less than the densities routinely found in loops from EUV and SXR diagnostics. Therefore, it seems unlikely that the majority of the plasma seen in white light CMEs at  $15 R_{\odot}$  originates from the low corona, if the adiabatic expansion assumption is valid. Moreover, the EUV images of the low corona show that densities can vary significantly (much more than an order of magnitude) from active region to active region and between active and quiet sun. This is not what our measurements show suggesting that plasmas at larger scales are involved.

The spread in the CME densities could be caused by departures of the CME shape from the spherical symmetry implied by the assumption of a LOS depth equal to the projected width. We can associate the density spread to a variation of the CME aspect ratio,  $K$ , defined as the ratio between its projected width over its LOS depth. In that case, the variation in  $K$  is proportional to the variation in density and therefore  $K \propto 3.8/2 = 1.9$ , in the outer corona. Interestingly, this value is consistent with forward modeling ratios in Thernisien et al. (2009) ( $K = \kappa / \sin \alpha$  in their notation) and flux-rope fitting by Krall & St. Cyr (2006) ( $K \approx (1 - \epsilon^2)^{1/2} \Lambda$  in their notation).

### 3.4. 'Pseudo-CMEs'

We now return to Figure 11. Why are there events that do not show a continuous mass increase as they expand in the outer corona but rather peak within  $7R_{\odot}$ ? We can think of several possibilities for such measurements: (i) unavailability of observations at higher heights (i.e., instrumental problems, spacecraft operations, special observing programs). (ii) Multiple event overlap which makes it difficult to follow the original event. This may be common during the solar activity peak. (iii) Extremely fast events which allow only a handful of observations in the LASCO coronagraph FOV. (iv) CMEs producing large amounts of prompt particles which in turn create a cosmic ray 'storm' on the detectors and hinder measurements, and finally (v) normal events that start bright in the C2 images but diffuse and later disappear in the C3 FOV for various reasons such as (v1) material draining back. (v2) They are located off-limb, so that the brightness falls off faster than

the background. (v3) They expand super-radially, thereby reducing the volume density, and (v4) part of the emission originates not from Thomson scattering but from other processes, most likely  $H\alpha$  emission.

The large number of these events (54% of the total sample) makes them unlikely to be due solely to erroneous measurements or missing observations. Besides, we have excluded from consideration all events with  $\leq 3$  HT points and all halos and partial halos which tend to be the fastest CMEs and most likely to be associated with particle storms. Therefore, some of these events exhibit a real decline of mass with height, either because of overlap with other CMEs or because of reasons (v1) to (v4) outlined above. Indeed, this is what we find when we look at some individual events in more detail (Figure 12). After an initial peak in the C2 FOV, the mass seems to decline rather rapidly until the event reaches background brightness and disappears within the FOV. Since we plot only the positive mass measurements, these points end well before the available height-time measurements (asterisks). An inspection of the mass images reveals quickly whether this is due to an event expanding into another CME. In that case, the preevent image may contain part of the preceding CME and will therefore have negative values in those locations which will result in negative measurements (e.g., 2000/08/12 and 2000/11/24 events). For the other two events, however, we find nothing unusual in the images. The CME simply becomes fainter as it expands in the C3 FOV. This behavior is different from usual CMEs (e.g., Figure 5 and Vourlidis et al. 2000) and thus we suspect that the nature of these events may be different. They may not be magnetically driven, for example. However, we cannot rule out the contribution from  $H\alpha$  within the C2 FOV since the C2 bandpass includes the  $H\alpha$  line. Many CMEs clearly contain filamentary material which is likely  $H\alpha$  when it is quite luminous (usually in small knots) in low heights. The material ionizes quickly and there are rarely any traces in the C3 FOV. Since our measurements are performed automatically, and many CMEs contain filamentary material it is reasonable to assume that for at least some CMEs the mass peak in low heights must be due to contributions from  $H\alpha$ .

Much more work is required to properly discriminate among all these possibilities and determine whether the number of events that are truly different than normal CMEs is significant. We, tentatively, refer to all events with mass peaks below  $7 R_{\odot}$  as ‘pseudo-CMEs’ to differentiate them from the rest of the sample since they do have very different properties. In Figure 13, we compare the mass and energy distributions of the two populations to the overall distributions of the sample. It is clear that the ‘pseudo-CMEs’ account for the low end tails of the distribution and have smaller masses and energies than the events above  $10R_{\odot}$ . A detailed analysis of these events requires a deeper ‘cleaning’ of the database to remove instrumental and other effects, as we mentioned above, and further examination of their evolution. Such analysis will detract from the focus of the current paper and will be presented in a forthcoming publication. The current discussion aims to make the reader aware that such events exist and that they may not be CMEs or, at least, not CMEs in the way we are accustomed to think of them.

### 3.5. Solar Cycle Effects

There have been numerous studies of CME properties in the past but they never extended over a full solar cycle. The almost uninterrupted LASCO observations for 13 years (so far) provide us with an unprecedented opportunity to study the variation of the CME properties through more than a cycle. CME properties such as speeds, widths, position angles and rates over various lengths of the recent solar cycle 23 have been presented before (Gopalswamy et al. 2004; Yashiro et al. 2004; Cremades & St. Cyr 2007; Gopalswamy et al. 2009). Here we concentrate on the mass and energy properties, expanding on our earlier report (Vourlidas et al. 2002). There has been an indication for a solar cycle dependence on the CME mass. (MacQueen et al. 2001) derived a factor of 4 increase in the CME mass between the minimum and maximum of cycle 23 but these results are based on partial cycle coverage. We plot the yearly average of CME mass as a function of time in the upper left panel of Figure 14. It is rather clear that the mass depends on the cycle although it remained relatively flat between 1997-2002. The average begins to decline in step-wise fashion in 2003 until 2007 when we start seeing an increase in the average mass. The current 2009 average ( $6 \times 10^{13}$  g) is still much lower (by  $4.6\times$ ) than the average in the previous minimum ( $2.8 \times 10^{14}$  g) in 1996.

This behavior becomes more visible if we consider the average mass density (upper right panel, Figure 14). There we see a continuous increase in the average CME density as the activity increases. Even the characteristic double-peaked shape of the sunspot number is reproduced in the plot. Starting in 2003, however, there is a sharp decline leading to a plateau in 2006. There is only a very small hint of increasing density in the 2009 data.

The decline does not correlate with the measured speed (middle right panel, Figure 14) which shows a good correlation with sunspot numbers. However, the average speed in 2009 (231 km/sec) is also lower than the average 1996 speed (276 km/sec) but the difference is much less pronounced than in the CME mass and density.

The CME kinetic energy, being the product of mass and the square of the speed, reflects the variation of both quantities. However, the mass varies by about a factor of 10 throughout the cycle and the speed varies only by a factor of  $\sim 2$ . So the kinetic energy is more influenced by the mass variations. There is a decline in CME energies in 2003 and a minimum in 2007. The current average kinetic energy ( $1.3 \times 10^{28}$  ergs) is  $6.4\times$  smaller than the average CME kinetic energy in 1996 ( $8.3 \times 10^{28}$  ergs).

#### 3.5.1. The Sharp Decline in CME Mass in mid-2003

To the best of our knowledge these behaviors have not been discussed before. To see whether this is an effect from the yearly averaging and to locate the time of the sharp decline in CME mass more precisely, we compute the total CME mass per Carrington rotation in the bottom panel of Figure 14. The plot corroborates our yearly statistics and shows some very interesting trends. The

mass increases with solar activity in an intermittent fashion of 2-3 months of high mass followed by periods of lower output (see also Figure 3 in Vourlidas et al. (2002)). The peak is reached in April-May 1998 and the monthly mass remains more or less constant thereafter. The drop seen in the late 1998 - early 1999 is due to the temporary loss of the SOHO spacecraft and other spacecraft emergencies until synoptic observations were reliably reestablished in March 1999. The monthly mass starts to decline in 2003 but then it suddenly drops by a factor of 10 between Carrington rotations 2004 and 2005 (marked by an arrow in Figure 14). This corresponds to the months of June and July of 2003.

We do not yet have a fully satisfying explanation for the sudden drop in 2003. It is not seen in the projected CME widths or the heights but there is a small hint of it in the ROI area. Our first suspect was the magnetic field polarity reversal. But that occurred in 2000-2001 and affected only the position angle of the events, apparently (Gopalswamy et al. 2003). The drop is very apparent in the mass density plot and less apparent on the energy plot. This is due to the different speed behavior. The CME speeds follow closely the two-peaked evolution in the sunspot numbers (Figure 14). This discrepancy suggests that the drop is more of a coronal density rather than a magnetic effect. Our ongoing analysis of the streamer brightness throughout the solar cycle shows the same behavior as the CME masses and corroborates our suggestion (Howard et al. 2009). On the other hand, the steepness of the drop may be exaggerated by observing interruptions due to spacecraft antenna problems during that period. SOHO started its 3-month 180° rolls at the end of the summer 2003. It may also be normal. The activity also peaked relatively quickly in 1998 during the rising phase of cycle 23. we do not have CME measurements over a sufficient number of solar cycles to make a definitive statement. We will continue to investigate this issue and will report our findings in a future publication.

### 3.5.2. *Six-month variability in CME mass*

After 2003, the CME mass shows large fluctuations over the scale of a few months until about 2006. The variability seems to be related to the appearance of large sunspot groups (e.g. ARs 10486-488 in the October-November 2003 period) but it also seems to be periodic. To look for periodicities in the mass data, we use the Lomb Normalized Periodogram (LNP) method which is robust against data gaps and readily available in IDL. The procedure has been developed as an alternative to Fourier transform analysis for working with unevenly spaced data and time series with data gaps (Lomb 1976; Scargle 1982) and is therefore appropriate for our data sample. The algorithm accepts as input the amplitude of a signal versus time, computes the periodogram and tests the hypothesis that a given frequency peak represents a significant periodic signal against the white noise hypothesis. The program returns the power of the signal as a function of frequency and the probability for each peak of arising from random noise. A low probability value denotes a significant periodic signal. We use the method as implemented in the IDL LNP\_TEST routine.

As input we take the average CME mass in 10-day bins. The resulting periodogram is shown

in Figure 15. We find a very significant peak at a period of 179.1 days. The probability of this peak being due to random noise is only  $3.7 \times 10^{-11}$ . To check for effects of binning, we repeated the analysis with different temporal bins without any change in the results. The peak remains at the same period. When we repeat the analysis on a yearly basis, we find that the 6-month peak arises only from 2003 onwards. We did not detect any significant peaks during the previous minimum in 1996-1999. The mission interruption and synoptic program changes during 1996-1997 may have played a role. We also searched for possible instrumental causes for this variability. It is, however, difficult to see how such a long-term periodicity can arise when we are dealing with essentially base-difference images taken a few hours apart. Spacecraft operations can also be dismissed since they occur on a 3-month basis and are subtracted out in any case when the pre-event image is subtracted. To find out when the activity peaks during the year, we calculated the average CME mass per calendar month for the whole database in figure 16. The 6-month variability is obvious in the plot and corresponds to the months of April-May and October-November. Indeed, these months are related to increased solar activity since the beginning of the SOHO mission (e.g., see numerous papers on November 1997, April-May 1998, October-November 2003 events).

This is the not the first time that a 6-month periodicity is reported. Lara et al. (2008) found a 193-day periodicity in a spectral analysis of CME rates from 1995 to 2006. Their sample included all events in the CDAW list so the 13-day difference with our results may stem from the inclusion of the smaller events or the use of rates instead of a physical property such as mass or both. A well-known '154-day' periodicity has been reported for many other solar activity indicators such as flares, sunspot numbers, ICME rates, flux emergence (see Richardson & Cane 2005, and references therein). Those studies have shown that the periodicity is quite wide and can extend from 154 to 190 days, depending on the analysis method. In our case, we could only detect the 180-day periodicity and there were no peaks in other periods (Figure 15). It may be that such periodicities change from cycle to cycle as suggested by Richardson & Cane (2005). In addition, there has not been a satisfactory explanation for the 154-day periodicity in the other solar parameters nor can we provide one for the 180-day periodicity in our data. We can only point out that our periodicity is directly related to the appearance of large active region complexes on the sun and therefore must be related to processes that control magnetic flux emergence from the convection zone. A similar conclusion was reached by Lara et al. (2008). More studies are surely necessary and may be able to provide new insights into the link between flux emergence and the CME ejection phenomenon.

We close this section by noting that starting in 2006, the monthly ejection rate shows less fluctuations but the 180-day periodicity persists. The rate has a slower downward trend and reaches activity levels similar to 1996-1997. In other words, the minima of cycles 22 and 23 are similar. The last point in this graph is unusually low because it contains only a third of the number of events (8 CMEs) in any of the previous points ( $> 20$ ).

#### 4. Conclusions

In the preceding sections, we presented an extensive analysis of the first full solar cycle database of CMEs from the viewpoint of their mass and energy properties. This work provided us with the opportunity to describe in detail the mass measurement procedures with their error analyses for the first time in the literature. Our measurements are incorporated in the online database of the LASCO PI team at NRL (<http://lasco-www.nrl.navy.mil/>) and our initial statistical analyses provided new insights on the interpretation of CME measurements and the nature of CMEs. We summarize the main results of our study as follows:

- We identify the existence of two populations in the mass CME data: The 'normal' CMEs which reach a constant mass beyond  $10 R_{\odot}$ , and the 'pseudo' CMEs which reach a mass peak below  $7 R_{\odot}$  before they disappear in the C3 field of view.
- The average CME mass density is remarkably constant for the 'normal' CMEs at  $\rho = 10^{12.83 \pm 0.25} \text{ g}/R_{\odot}^2$ . Therefore, one can calculate the mass of any CME, within a factor of 3, simply by multiplying this density with the projected area of the CME, in  $R_{\odot}^2$ , as measured in the images. The CME volumetric density, calculated under the assumption of line-of-sight width equal to the observed width, is  $\sim 3500 \text{ cm}^{-3}$  and suggests that most of the CME mass originates in the high corona, if CMEs expand adiabatically.
- The mass and energy distributions become log-normal only for measurements at around 10-15  $R_{\odot}$ . The implication is that measurements at lower heights provide an incomplete picture of the event and will bias statistical studies. Coronagraphs with FOVs at or beyond  $15 R_{\odot}$  are essential for CME studies.
- We show the first complete solar cycle behavior of the CME mass, density, and energies. The statistics reveal a sudden drop in the CME mass, mass density, and energy which takes place within two Carrington rotations (2005-2006) in June-August, 2003. This is followed by an increased monthly variability in these CME properties that lasts until mid-2005 with a very strong 6-month periodicity which continues to this day. The reason for this sudden change is unclear at this moment but it seems to signal a transition of the large scale coronal electron content towards minimum levels. The cause of the 6-month variability is also under investigation.
- We show that the CME properties also vary between cycles. CMEs seem to be less massive (by almost a factor of 10) compared to cycle 21 measurements. Also, the CME properties at the current minimum are below their values in the previous minimum by factors of 4.6 for the mass, 6.4 for the energy and only 17% for the speed. These observations provide additional evidence for the unusual minimum of cycle 23.
- The LASCO duty cycle is  $\sim 94\%$ .

- Instrumental errors and assumptions on the composition of the plasma are insignificant compared to the projection errors below.
- CME masses and potential energies may be underestimated by a maximum of 2x, and the kinetic energies by a maximum of 8x (mostly due to the speed projection).

The above results constitute only a subset of the possible analyses that can be performed with such a large dataset of CME measurements. The current analysis has established some of the typical properties, such as the typical CME density, mass flux, and the distribution of CME energies and masses and has raised new questions regarding the solar cycle variation of CME mass. We plan to continue updating the database while the operation of the LASCO coronagraphs continues.

SOHO is an international collaboration between NASA and ESA. LASCO was constructed by a consortium of institutions: the Naval Research Laboratory (Washington, DC, USA), the Max-Planck-Institut für Aeronomie (Katlenburg-Lindau, Germany), the Laboratoire d’Astronomie Spatiale (Marseille, France) and the University of Birmingham (Birmingham, UK). The LASCO CME catalog is generated and maintained at the CDAW Data Center by NASA and The Catholic University of America in cooperation with the Naval Research Laboratory.

## REFERENCES

- Abramenko, V. I., & Longcope, D. W. 2005, *ApJ*, 619, 1160
- Andrews, M. D., Wang, A., & Wu, S. T. 1999, *Sol. Phys.*, 187, 427
- Aoki, S., Yashiro, S., & Shibata, K. 2003, in *International Cosmic Ray Conference*, Vol. 5, *International Cosmic Ray Conference*, 2729–+
- Bewsher, D., Harrison, R. A., & Brown, D. S. 2008, *A&A*, 478, 897
- Billings, D. E. 1966, *A guide to the solar corona* (New York: Academic Press Inc)
- Brueckner, G. E., et al. 1995, *Sol. Phys.*, 162, 357
- Ciaravella, A., Raymond, J. C., van Ballegoijen, A., Strachan, L., Vourlidas, A., Li, J., Chen, J., & Panasyuk, A. 2003, *ApJ*, 597, 1118
- Colaninno, R. C., & Vourlidas, A. 2009, *ApJ*, 698, 852
- Cremades, H., & St. Cyr, O. C. 2007, *Advances in Space Research*, 40, 1042
- Crow, E. L., & Shimizu, K. 1988, *Lognormal Distributions: Theory and Applications* (New York: Marcel Dekker, Inc)

- Domingo, V., Fleck, B., & Poland, A. I. 1995, *Sol. Phys.*, 162, 1
- Filippov, B., & Koutchmy, S. 2002, *Sol. Phys.*, 208, 283
- Gilbert, H. R., Serex, E. C., Holzer, T. E., MacQueen, R. M., & McIntosh, P. S. 2001, *ApJ*, 550, 1093
- Gopalswamy, N., Lara, A., Yashiro, S., & Howard, R. A. 2003, *ApJ*, 598, L63
- Gopalswamy, N., Nunes, S., Yashiro, S., & Howard, R. A. 2004, *Advances in Space Research*, 34, 391
- Gopalswamy, N., Yashiro, S., Michalek, G., Stenborg, G., Vourlidas, A., Freeland, S., & Howard, R. 2009, *Earth Moon and Planets*, 104, 295
- Hayes, A. P., Vourlidas, A., & Howard, R. A. 2001, *ApJ*, 548, 1081
- Hildner, E., Gosling, J. T., MacQueen, R. M., Munro, R. H., Poland, A. I., & Ross, C. L. 1975, *Sol. Phys.*, 42, 163
- Howard, R. A., Battams, K., Vourlidas, A., Morrill, J. S., & Stenborg, G. 2009, *AGU Fall Meeting Abstracts*, C4+
- Howard, R. A., Sheeley, Jr., N. R., Michels, D. J., & Koomen, M. J. 1985, *J. Geophys. Res.*, 90, 8173
- Hundhausen, A. J. 1993, *Journal of Geophysical Research*, 98, 13177
- Hundhausen, A. J., Stanger, A. L., & Serbicki, S. A. 1994, in *ESA Special Publication*, Vol. 373, *Solar Dynamic Phenomena and Solar Wind Consequences, the Third SOHO Workshop*, ed. J. J. Hunt, 409–+
- Jackson, B. V., & Howard, R. A. 1993, *Sol. Phys.*, 148, 359
- Kahler, S. W., & Vourlidas, A. 2005, *Journal of Geophysical Research (Space Physics)*, 110, 12
- Krall, J., & St. Cyr, O. C. 2006, *The Astrophysical Journal*, 652, 1740
- Lara, A., Borgazzi, A., Mendes, Jr., O., Rosa, R. R., & Domingues, M. O. 2008, *Sol. Phys.*, 248, 155
- Limpert, E., Stahel, W. A., & Abbt, M. 2001, *BioScience*, 51, 341
- Llebaria, A., Lamy, P., & Danjard, J. 2006, *Icarus*, 182, 281
- Lomb, N. R. 1976, *Ap&SS*, 39, 447
- Lugaz, N., Manchester, IV, W. B., & Gombosi, T. I. 2005, *ApJ*, 627, 1019



- MacQueen, R. M., Burkepile, J. T., Holzer, T. E., Stanger, A. L., & Spence, K. E. 2001, *ApJ*, 549, 1175
- Mittal, N., Pandey, K., Narain, U., & Sharma, S. S. 2009, *Astrophysics and Space Science*, 323, 135
- Morrill, J. S., et al. 2006, *Sol. Phys.*, 233, 331
- Poland, A. I., Howard, R. A., Koomen, M. J., Michels, D. J., & Sheeley, Jr., N. R. 1981, *Sol. Phys.*, 69, 169
- Reinard, A. A. 2008, *ApJ*, 682, 1289
- Reiner, M. J., Vourlidas, A., Cyr, O. C. S., Burkepile, J. T., Howard, R. A., Kaiser, M. L., Prestage, N. P., & Bougeret, J. 2003, *ApJ*, 590, 533
- Richardson, I. G., & Cane, H. V. 2005, *Geophys. Res. Lett.*, 32, 2104
- Robbrecht, E., Patsourakos, S., & Vourlidas, A. 2009, *ApJ*, 701, 283
- Scargle, J. D. 1982, *ApJ*, 263, 835
- Sheeley, Jr., N. R., et al. 1997, *ApJ*, 484, 472
- St. Cyr, O. C., et al. 2000, *J. Geophys. Res.*, 105, 18169
- Stewart, R. T., McCabe, M. K., Koomen, M. J., Hansen, R. T., & Dulk, G. A. 1974, *Solar Physics*, 36, 203
- Subramanian, P., & Vourlidas, A. 2007, *A&A*, 467, 685
- Thernisien, A., Vourlidas, A., & Howard, R. A. 2009, *Sol. Phys.*, 256, 111
- Vourlidas, A., Buzasi, D., Howard, R. A., & Esfandiari, E. 2002, in *ESA Special Publication*, Vol. 506, *Solar Variability: From Core to Outer Frontiers*, ed. J. Kuijpers, 91–94
- Vourlidas, A., & Howard, R. A. 2006, *ApJ*, 642, 1216
- Vourlidas, A., Subramanian, P., Dere, K. P., & Howard, R. A. 2000, *ApJ*, 534, 456
- Yashiro, S., Gopalswamy, N., Michalek, G., & Howard, R. A. 2003, *Advances in Space Research*, 32, 2631
- Yashiro, S., Gopalswamy, N., Michalek, G., St. Cyr, O. C., Plunkett, S. P., Rich, N. B., & Howard, R. A. 2004, *Journal of Geophysical Research (Space Physics)*, 109, 7105
- Yurchyshyn, V., Yashiro, S., Abramenko, V., Wang, H., & Gopalswamy, N. 2005, *ApJ*, 619, 599

Table 1. Typical Errors in the Calculation of CME Mass

Operation	Parameter	$\sigma_x/x(\%)$
DN $\rightarrow$ MSB: $I = \frac{S}{t} * V * F_{cal}$	I	1.98 – 2.3
	S	0.4 - 1.4
	t	0.15
	V	1
	$F_{cal}$	0.73
MSB $\rightarrow$ excess MSB: $I_{CME} = I - I_{pre}$	$I_{CME}$	4 <sup>a</sup>
	$I_{CME}$	0.005 <sup>b</sup>
Excess MSB $\rightarrow$ Mass: $M_{CME} = I_{CME} * C_e * C_{plasma}$	$M_{CME}$	100.2
	$C_e$	-100
	$C_{plasma}$	-6

<sup>a</sup>Assuming independent variables

<sup>b</sup>Based on C3 data (Figure 2)

Table 2. Mass and Energy Properties of CMEs (1996-2009)

Property	LASCO			Solwind
	Histogram Peak	Average	Median	Average
Mass ( $\times 10^{14}$ g)	3.4	3.9	11	17
$E_K$ ( $\times 10^{29}$ ergs)	3.4	2.3	19	43
$E_{mech}$ ( $\times 10^{29}$ ergs)	8.5	9.0	38	...
Total Mass ( $\times 10^{18}$ g)	...	...	9.2	3.9
Mass Flux ( $\times 10^{15}$ g/day)	...	...	1.8 <sup>a</sup>	7.5
Duty Cycle	...	...	94%	61.7%

<sup>a</sup>1996-2003:  $2.6 \times 10^{15}$  g/day. 2003-2009:  $8.3 \times 10^{14}$  g/day.

Table 3. Results of the Normal Fit to the log of Mass and Energy

Parameter	$\mu$	Geometric Mean ( $e^\mu$ )	$\sigma$
Mass (g)	34.974	$1.55 \times 10^{15}$	1.114
$E_K$ (ergs)	69.748	$1.96 \times 10^{30}$	1.515
$E_{mech}$ (ergs)	70.682	$4.98 \times 10^{30}$	1.184

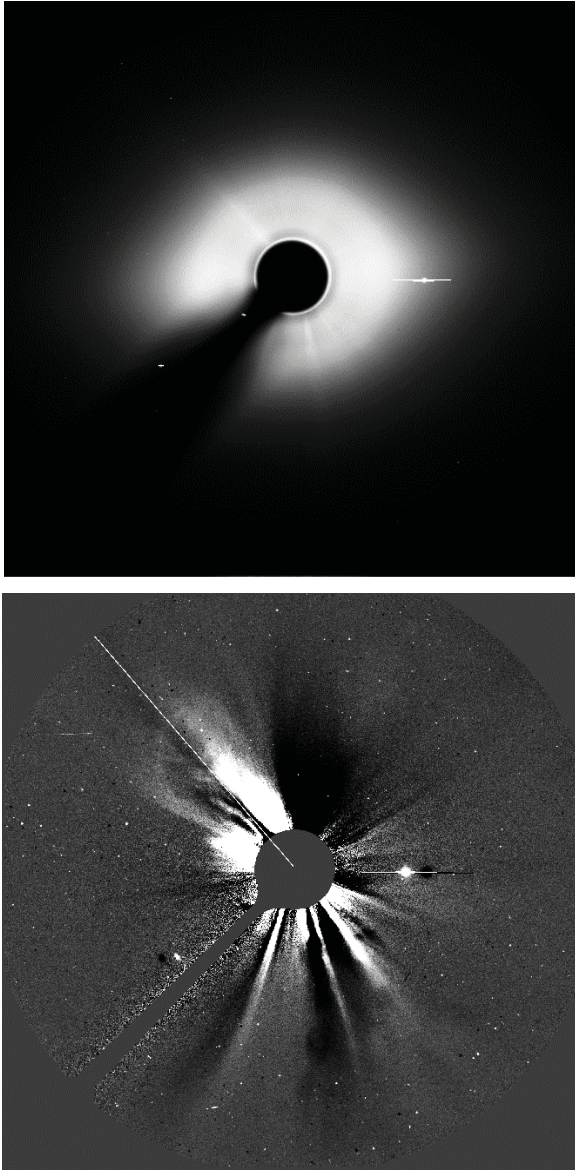


Fig. 1.— *Top panel:* A typical LASCO/C3 image of a CME as received on the ground. *Bottom panel:* An excess mass image produced by the image above after removal of the F-corona, instrumental effects and the subtraction of a pre-event image. The solid line marks the position angle of the radial brightness profile we use in our analysis.

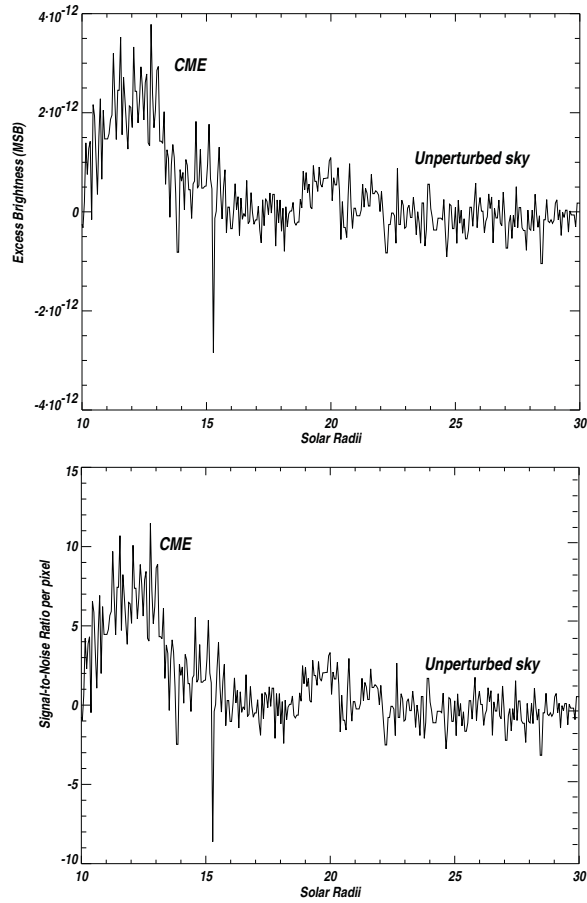


Fig. 2.— *Top panel:* A typical radial profile of excess brightness. The CME and background sky levels are shown. The units are in MSB per pixel. *Bottom panel:* The same plot in units of SNR per pixel. The position angle of the brightness profile is shown in Figure 1.

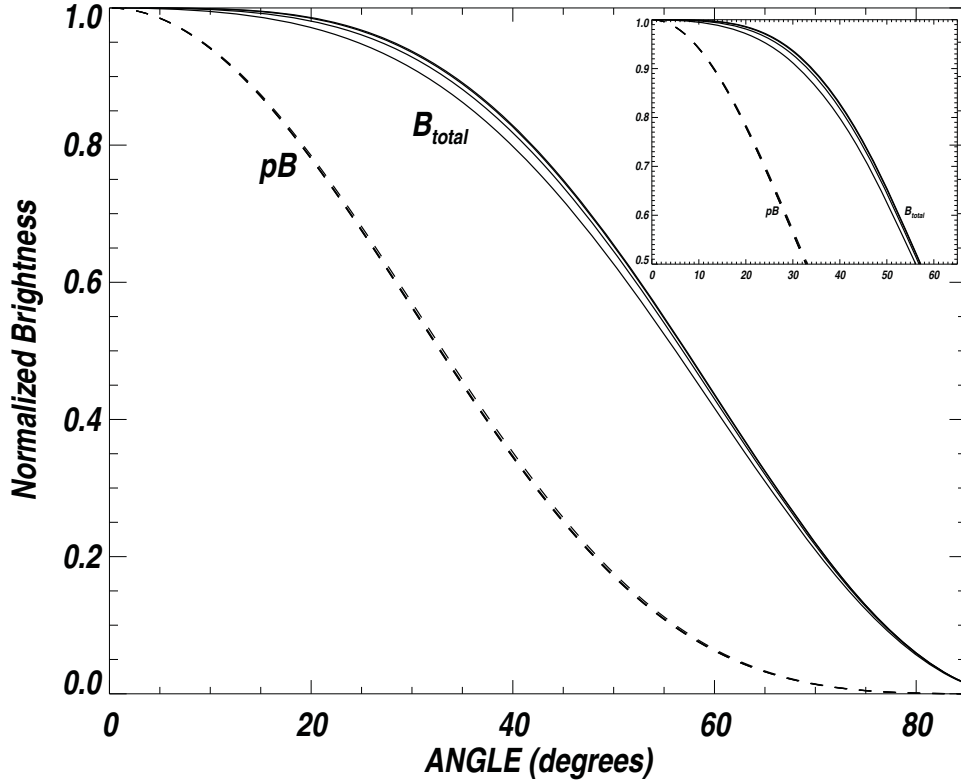


Fig. 3.— Angular dependence of the Thomson scattering brightness of a single electron at four impact distances (3, 5, 10, 20  $R_{\odot}$ ) for total (solid lines) and polarized (dashed lines) brightness. The brightness is normalized to the maximum at the sky plane ( $0^{\circ}$ ). The inner curves of total brightness correspond to smaller impact radii. The corresponding pB curves are indistinguishable from each other. *Insert:* Detail showing only brightnesses  $> 50\%$  of the maximum. See § 2.1.3 for details.

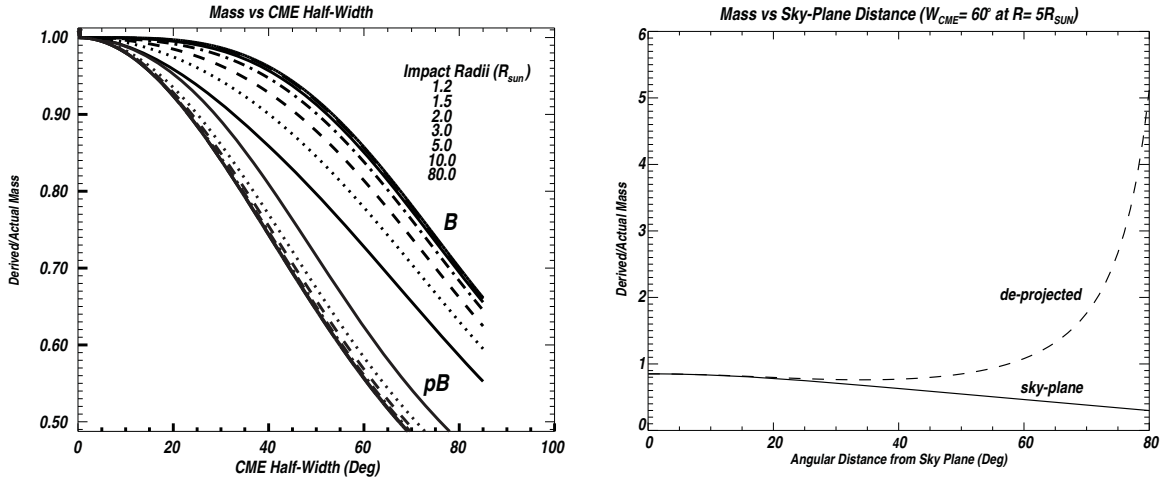


Fig. 4.— *Left*: Estimation of the error in the CME mass as a function of CME half-width. The CME is assumed to be a cone propagating along the sky plane. The error for both total and polarized brightness measurements and for a number of heliocentric distances is shown. *Right*: Estimation of the error in the CME mass as a function of CME angular distance from sky plane. The estimates are based on a  $60^\circ$ -wide CME and correspond to two cases; the standard assumption of all mass on the sky plane (curve labeled 'sky-plane') and taking into account the CME angle of propagation (curve labeled 'de-projected').

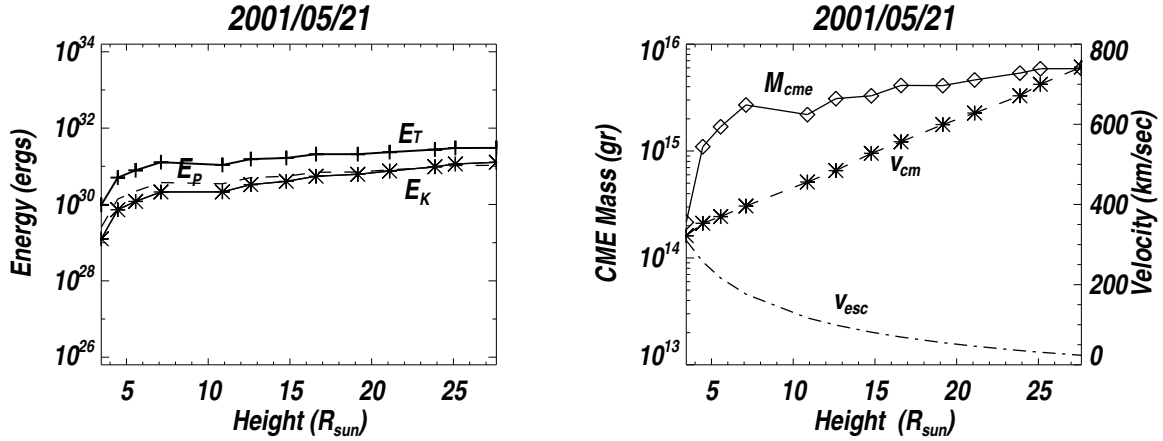


Fig. 5.— *Left*: Height evolution of the CME energy; : kinetic ( $E_K$ ), potential ( $E_P$ ), and total mechanical ( $E_K + E_P$ ). *Right*: Height evolution of the CME mass ( $M_{cme}$ ) and center-of-mass speed ( $v_{cm}$ ). The solar escape speed ( $v_{esc}$ ) is also shown.

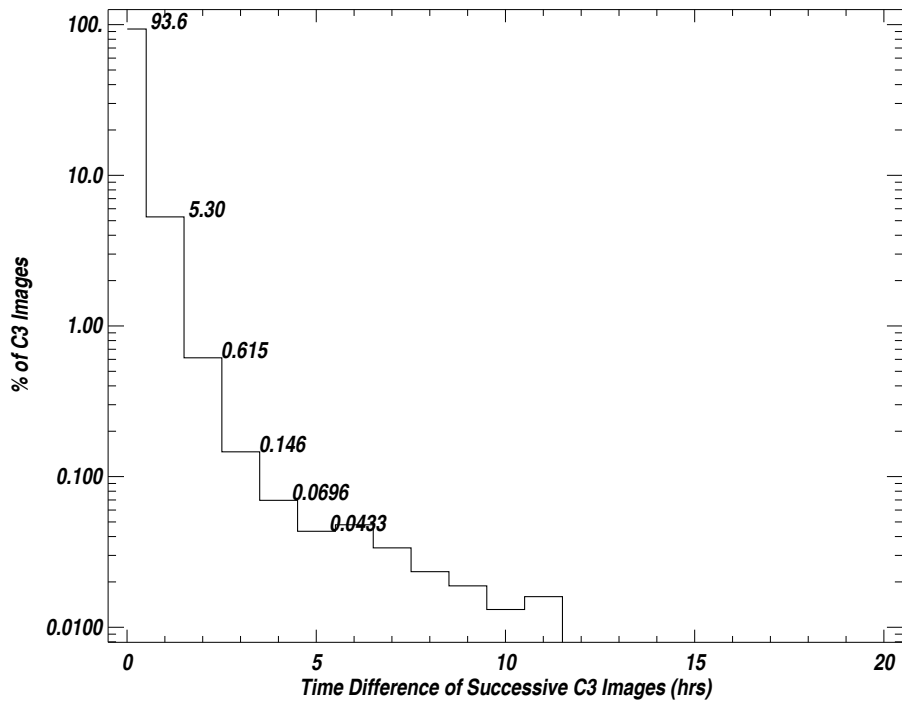


Fig. 6.— Histogram distribution of the C3 image cadence from 1996 to mid-2009. The sample contains all 175,361 synoptic images. The bin size is one hour. The percentage of images in the first five bins is printed on the plot and shows that 98.9% of all C3 images are taken within two hours of each other.



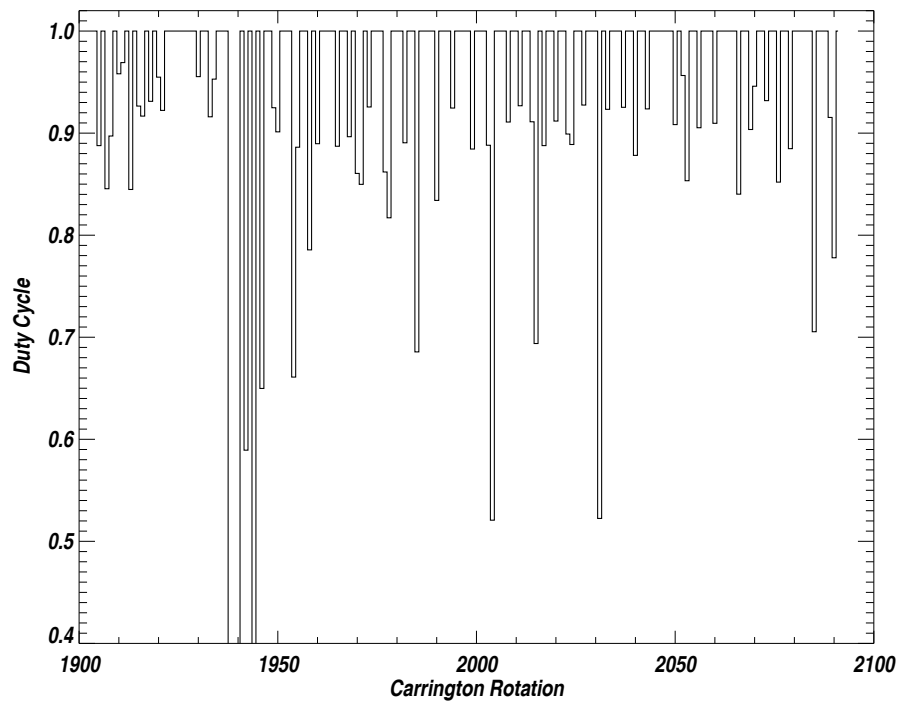


Fig. 7.— The C3 duty cycle per Carrington rotation. The plot is based on the percentage of  $> 18$  hrs data gaps. even the slowest CMEs ( $\sim 100$  km/s) will be missed with such data gap.

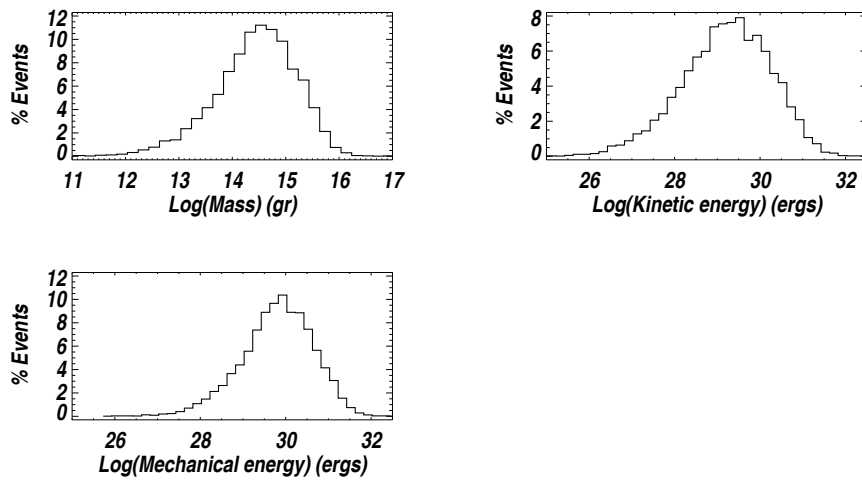


Fig. 8.— Histograms of CME mass distribution (upper left), kinetic energy (upper right) and total mechanical energy (bottom left) for all 7668 events in our database.

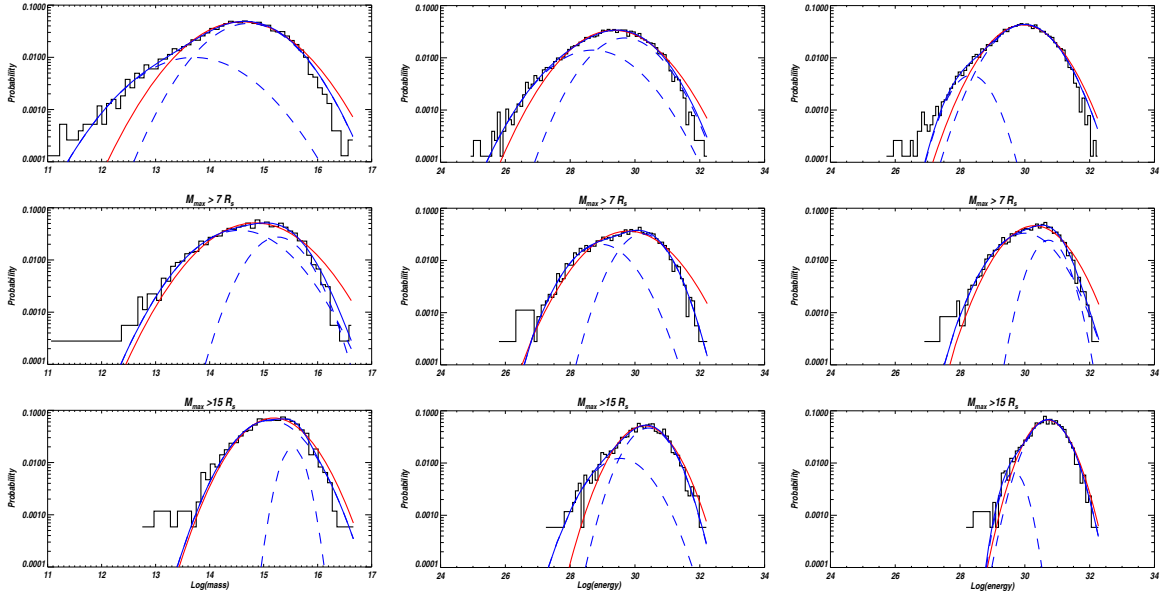


Fig. 9.— Top: Histograms of the logarithms of the distributions of CME mass (left), kinetic energy (center) and total mechanical energy (right) for all 7668 events. The red lines are single Gaussian fits. The blue lines are two-component Gaussian fits and the dotted blue lines show the individual Gaussians of the two-component fit. Considering events with mass maxima at increasing heights,  $7R_{\odot}$  (3579 events, middle),  $15R_{\odot}$  (1704 events, bottom), makes the measurements more consistent with a normal distribution of a single population rather than a two-population distribution. See Section 3.2 for details.

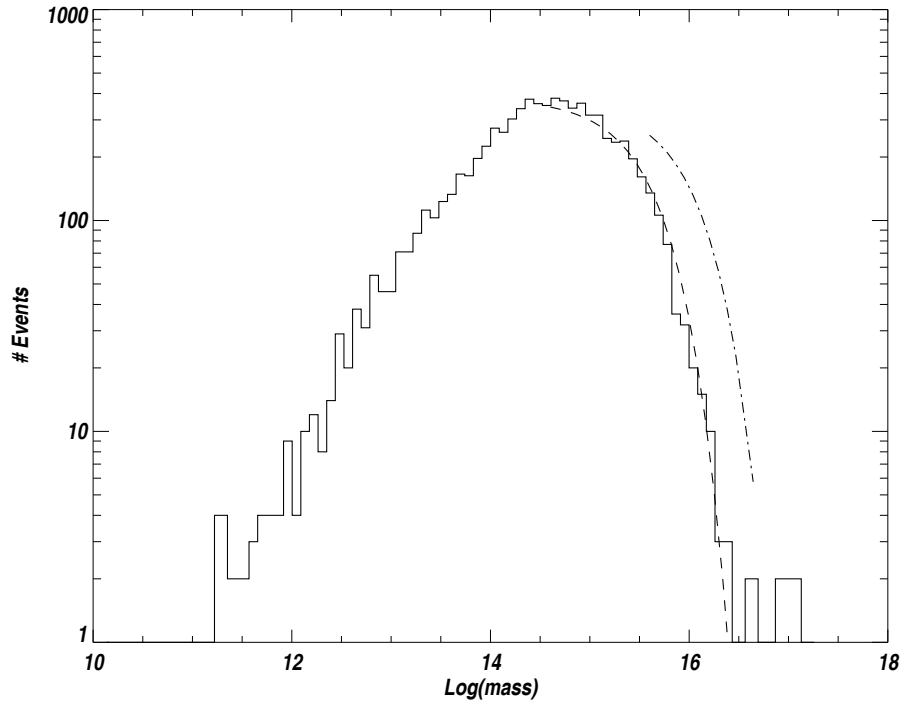


Fig. 10.— Comparison of the exponential CME mass distribution derived by Jackson & Howard (1993) from *Solwind* measurements ( $4 \times 10^{16} \geq M \geq 4 \times 10^{15}$  g) (dash-dotted line) to the LASCO measurements reported here. The dashed line is our exponential fit to  $4 \times 10^{16} \geq M \geq 5 \times 10^{14}$  g.

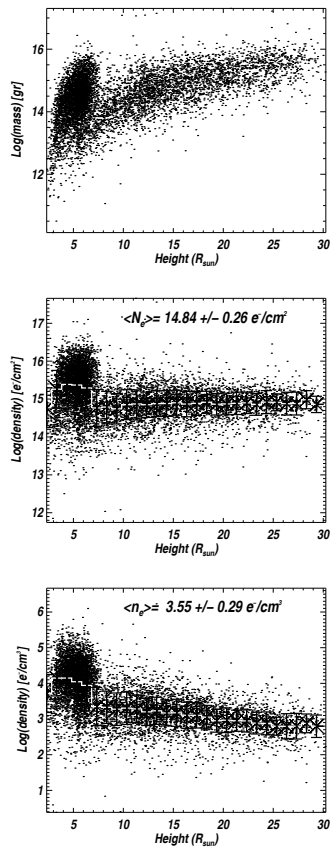


Fig. 11.— *Top*: Scatterplot of the logarithm of maximum CME mass versus the height where it was

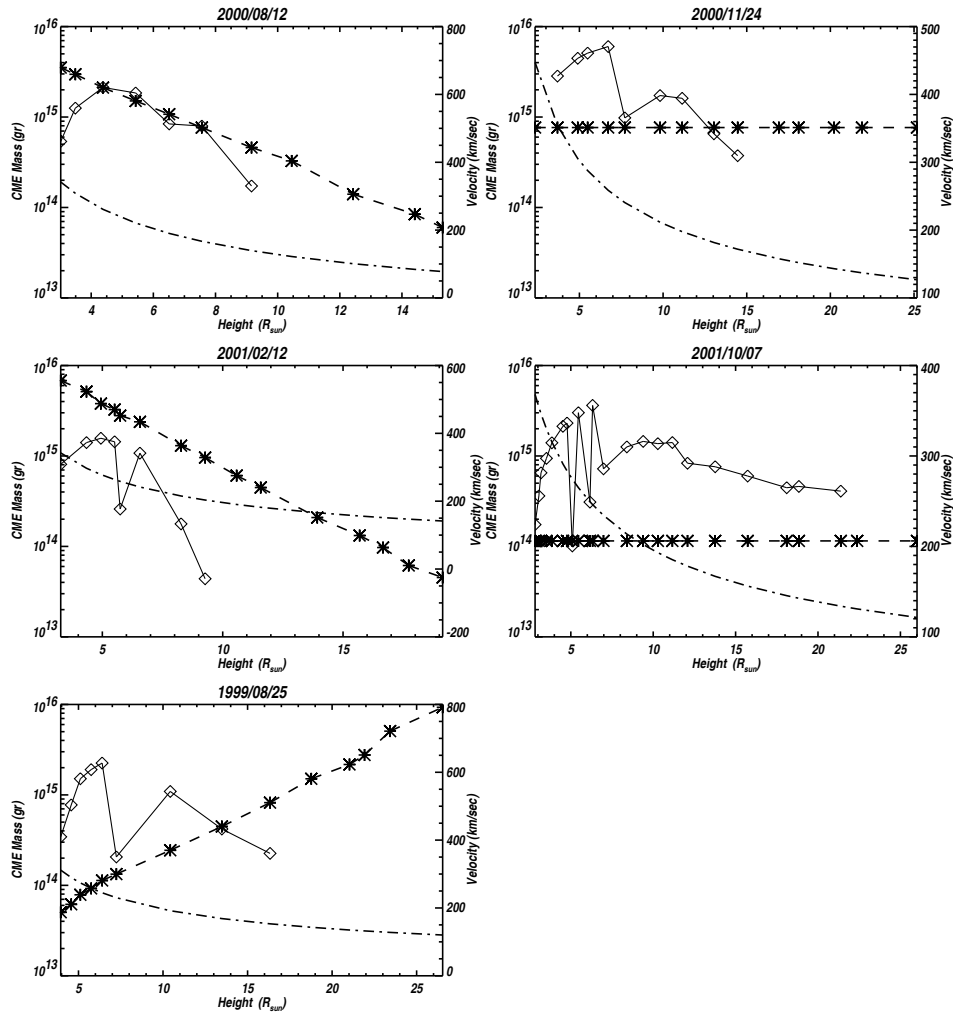


Fig. 12.— Mass and speed evolution of events selected from the 'pseudo'-CME population. The mass declines with height after reaching a peak in the inner corona but the events have speeds above the escape speed. Mass (solid line + diamonds), center-of-mass speed (dash + asterisks), escape speed (dash-dot). The difference in the number of mass and speed data points is due to the plotting of all speed but only positive mass measurements.

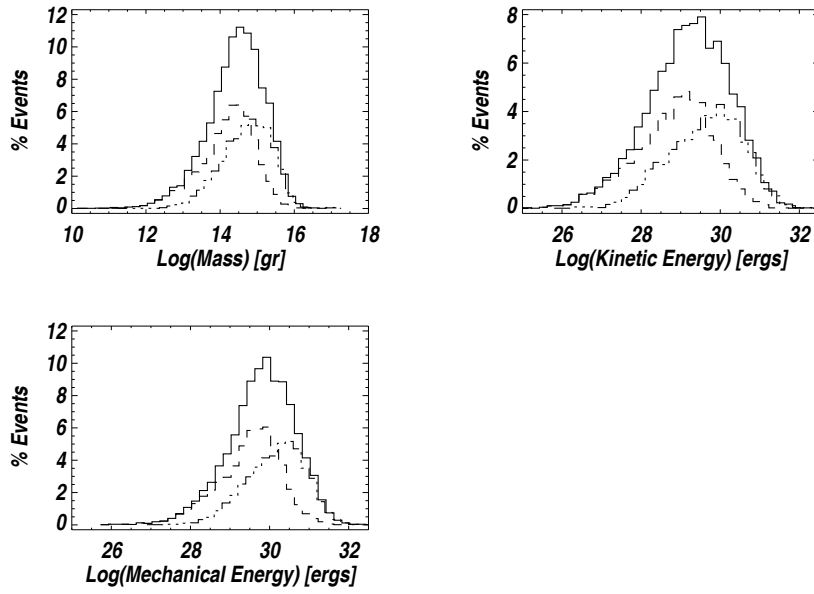


Fig. 13.— Same as Figure 8. Also shown are the histograms for events reaching maximum mass  $< 7R_{\odot}$  (dashed lines) and events reaching maximum mass  $\geq 7R_{\odot}$  (dash-double dot).

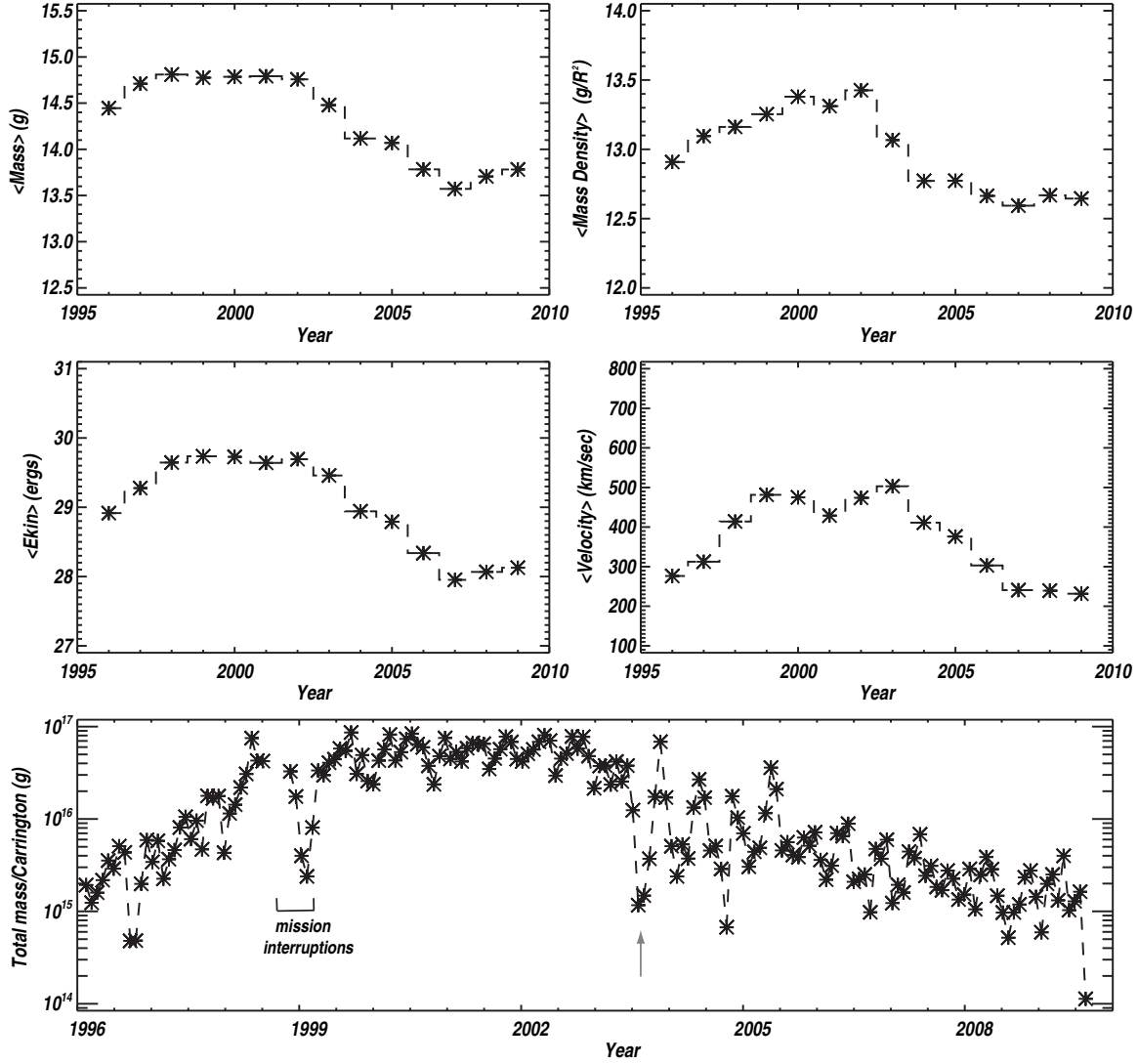


Fig. 14.— The solar cycle dependence of the CME mass and kinetic energy. *Top left:* Log CME mass. *Top right:* Log CME mass density in  $\text{g}/R_{\odot}^2$ . *Middle left:* Log CME kinetic energy. *Middle right:* CME speed. All four plots show yearly averages. *Bottom panel:* Total CME mass per Carrington rotation. The data gaps in 1998 and the drop in 1999 are due to spacecraft emergencies. The pronounced change in the mass variability (arrow) after the middle of 2003 is of solar origin but not fully understood yet.



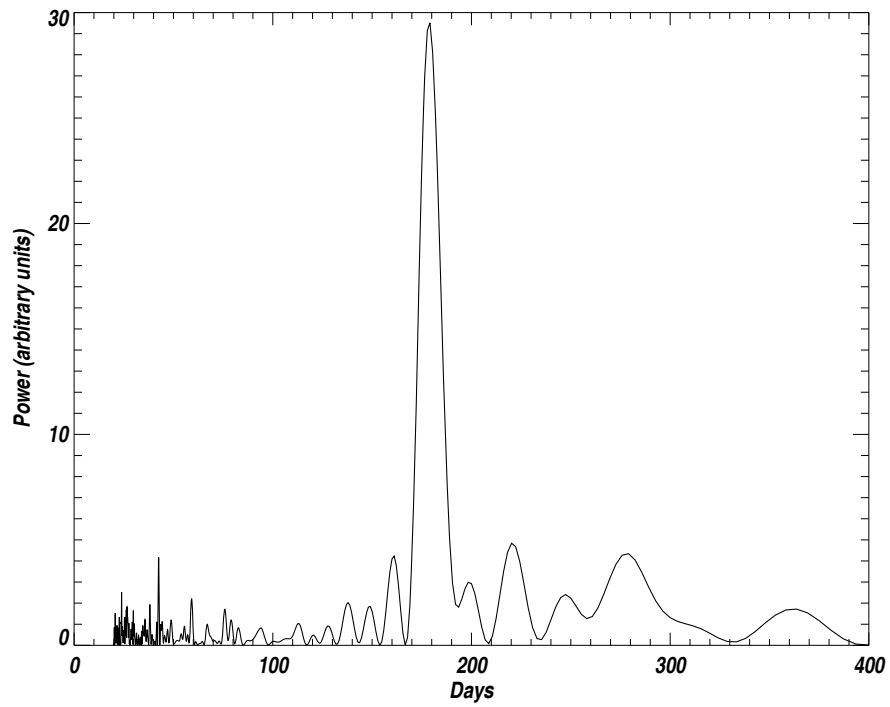


Fig. 15.— Lomb-Normalized periodogram for CME mass measurements in 2003 - 2009. The x-axis is labeled in days and the y-axis is the power of the peak. The measurements are binned in 10-day bins. There is a very significant peak at 179.1 days. The probability of being a random peak is  $3.7 \times 10^{-11}$ .

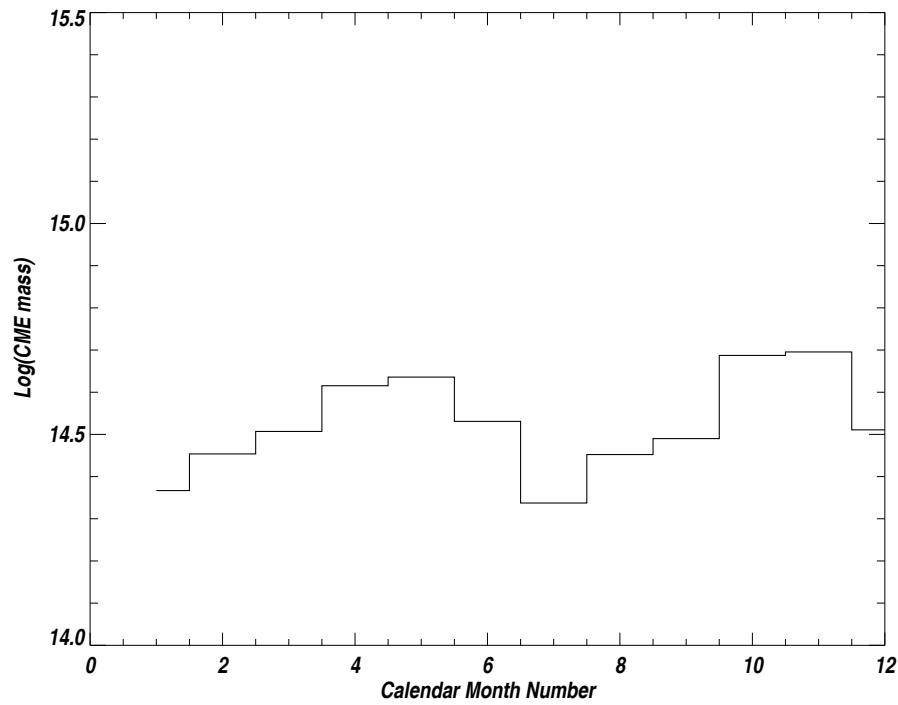


Fig. 16.— The logarithm of the average CME mass per calendar month is plotted for the full CME database. The graph suggests that the 6-month variability shown in Figure 15 originates in the months of April-May and October-November.